On the potential use of highly oxygenated organic molecules (HOM) as indicators for ozone formation sensitivity

Jiangyi Zhang[1], Jian Zhao[1], Yuanyuan Luo[1], Valter Mickwitz[1], Douglas Worsnop[1,2], and Mikael Ehn[1]

[1]Institute for Atmospheric and Earth System Research/Physics, Faculty of Science, University of Helsinki, Helsinki, 00014, Finland

[2]Aerodyne Research Inc., Billerica, Massachusetts, 01821, United States

Correspondence: Jian Zhao (jian.zhao@helsinki.fi) and Jiangyi Zhang (jiangyi.zhang@helsinki.fi)

Abstract. Ozone (O_3), an important and ubiquitous trace gas, protects lives from harm of solar ultraviolet (UV) radiation in the stratosphere but is toxic to living organisms in the troposphere. Additionally, tropospheric O_3 is a key oxidant, and source of other oxidants (e.g., OH and NO_3 radicals) for various volatile organic compounds (VOC). Recently, highly oxygenated organic molecules (HOM) were identified as a new compound group formed from oxidation of many VOC, making up a significant source of secondary organic aerosol (SOA). The pathways forming HOM from VOC involve autoxidation of peroxy radicals (RO_2), formed ubiquitously in many VOC oxidation reactions. The main sink for RO_2 is bimolecular reactions with other radicals, HO_2, NO or other RO_2, and this largely determines the structure of the end products. Organic nitrates form solely from RO_2 + NO reactions while accretion products ("dimers") solely from RO_2 + RO_2 reactions. The RO_2 + NO reaction also converts NO into NO_2, making it a net source for O_3 through NO_2 photolysis.

There is a highly nonlinear relationship between O_3, NO_x, and VOC. Understanding the O_3 formation sensitivity to changes in VOC and NO_x is crucial for making optimal mitigation policies to control O_3 concentrations. However, determining the specific O_3 formation regimes (either ~~VOC-limited~~ VOC- or NO_x-limited) remains challenging in diverse environmental conditions. In this work we assessed whether HOM measurements can function as a real-time indicator for the O_3 formation sensitivity based on the hypothesis that HOM compositions can describe the relative importance of NO as a terminator for RO_2. Given the fast formation and short lifetimes of the low-volatile HOM (timescale of minutes), they describe the instantaneous chemical regime of the atmosphere. In this work, we conducted a series of monoterpene oxidation experiments in our chamber while varying the concentrations of NO_x and VOC under different NO_2 photolysis rates. We also measured the relative concentrations of HOM of different types (dimers, nitrate-containing monomers, and non-nitrate monomers) and used ratios between these to estimate the O_3 formation sensitivity. We find that for this simple system, the O_3 sensitivity could be described very well based on the HOM measurements. Future work will focus on determining to what extent this approach can be applied in more complex atmospheric environments. Ambient measurements of HOM have become increasingly common during the last decade, and therefore we expect that there already are a large amount groups with available data for testing this approach.

1 Introduction

Ozone (O_3), as a key trace gas in the atmosphere, directly and indirectly affects human lives, and it plays diametrically opposed roles in the troposphere ("bad" ozone) and stratosphere ("good" ozone) (Sandermann, 1996; Staehelin et al., 2001; Seviour, 2022). The formation and depletion of O_3 has been investigated over the past decades (Chapman, 1930; Crutzen, 1970, 1971; Stolarski and Cicerone, 1974; Tiao et al., 1975; Dodge, 1977). Atmospheric O_3 is almost entirely produced through the reaction between atomic oxygen (O^3P) and molecular oxygen (O_2) (Wang et al., 2017). In the stratosphere, the O^3P source is O_2 photolysis with ultraviolet (UV) wavelengths below 240 nm (Chapman, 1930). Stratospheric O_3, which constitutes approximately 90% of Earth's atmospheric O_3, plays a crucial role in absorbing UV radiation in the UVB band (~~280–315~~ 280–315 nm), protecting organisms on the ground from the harm of UV radiation (Gruijl and Leun, 2000; Seinfeld and Pandis, 2016). Although certain man-made substances, such as chlorofluorocarbons, were found to be responsible for significant depletion of stratospheric O_3, the implementation of the 1987 Montreal Protocol and its subsequent amendments has contributed to the recovery of the stratospheric O_3 layer (Seinfeld and Pandis, 2016; Chipperfield et al., 2017).

In the troposphere, in addition to its role as a greenhouse gas (Ehhalt et al., 2001), O_3 serves as a secondary air pollutant due to its detrimental impacts and indirect emissions (Seinfeld and Pandis, 2016; Nuvolone et al., 2018). Not only is it toxic, but it also participates in chemical reactions that lead to the formation of other harmful molecules (Nuvolone et al., 2018). In contrast to stratospheric O_3 ~~,~~in the troposphere, the source of O^3P is NO_2 photolysis at wavelengths less than 420 nm (Madronich et al., 1983). However, the net formation of tropospheric O_3 occurs through chemical reactions involving nitrogen oxides (NO_x=NO+NO_2) and various volatile organic compounds (VOC) in the presence of UV light (Lelieveld and Dentener, 2000). In an ideal "clean" system without any VOC, once O_3 is formed, it readily converts NO back to NO_2 by reacting with NO, resulting in a null cycle as shown below (also illustrated as "NO_x cycle" in Fig. A1):

$$NO_2 + h\nu \xrightarrow{O_2} NO + O_3 \quad \text{R1}$$

$$O_3 + NO \rightarrow NO_2 + O_2 \quad \text{R2}$$

When VOC are present, they will be oxidized to form peroxy radicals (RO_2) by atmospheric oxidants, such as O_3 and OH (Atkinson and Arey, 2003):

$$VOC + oxidant \xrightarrow{O_2} RO_2 \quad \text{R3}$$

The RO_2 radicals can thus replace O_3 in converting NO into NO_2 (R4a). Some fraction of RO_2 + NO reactions will also lead to the formation of organic nitrates, $RONO_2$ (R4b) (Atkinson and Arey, 2003):

$$RO_2 + NO \rightarrow RO + NO_2 \quad \text{R4a}$$

$$\rightarrow RONO_2 \quad \text{R4b}$$

In summary, the presence of RO_2 radicals, supplied by VOC, can perturb the "NO_x cycle", leading to the net increase of O_3 (Fig. A1). As one of the most characteristic features of the photochemical smog episodes in many cities (Tiao et al., 1975; Tang

et al., 1995; Dickerson et al., 1997), this O_3 formation process (R1-~~R~~ R4a, Fig. A1), known as O_3-NO_x-VOC sensitivity or O_3 formation sensitivity, has been investigated since the last century (Haagen-Smit et al., 1953; Kinosian, 1982). The Empirical Kinetic Modeling Approach (EKMA) curve, namely O_3 isopleths, was proposed by Dodge (1977) and has been widely used to visually study the O_3 formation sensitivity (Liu and Shi, 2021). The O_3 isopleths reveal a highly nonlinear response of O_3 to its precursors, demonstrating that the impact on O_3 formation by reducing or increasing either VOC or NO_x does not consistently exhibit the same behavior (Meyer Jr et al., 1977; Harris et al., 1982; Sillman et al., 1990). The outcome is dependent on the relative concentrations of VOC (as a surrogate for RO_2) and NO_x, leading to the division of the formation area into NO_x-limited and VOC-limited regimes (Sillman, 1999; Melkonyan and Kuttler, 2012). In the NO_x-limited regime, the concentration of O_3 generally increases with an increase in NO_x, while its response to ~~changes in VOC~~ VOC changes remains relatively small. This is because the supply of RO_2 species from VOC is abundant and R4a is limited by NO (the "NO_x cycle" is saturated in Fig. A1). Conversely, in the VOC-limited regime, an increase in VOC concentration generally leads to an increase in O_3, whereas an increase in NO_x may even result in a decrease in O_3 levels. This is because NO_x is in excess compared to RO_2. Moreover, very high levels of NO_x can directly titrate O_3 (Sillman, 1999) or consume OH radicals (Atkinson et al., 2004), thereby reducing the supply of RO_2 species (R3) and promoting the reaction R2, which results in a decrease in the O_3 concentration. These effects were demonstrated by the amplified O_3 pollution in cities during ~~the~~ COVID-19 lockdown, when NO_x emissions dropped dramatically (Sicard et al., 2020).

To mitigate the uncertainties associated with photochemical models and efficiently determine the O_3 formation sensitivity, various photochemical indicators have been utilized since the last century ~~.~~(Wang et al., 2017; Liu and Shi, 2021). For example, the O_3 production efficiency (OPE = $\frac{\Delta O_3}{\Delta NO_z}$) is defined as the number of O_3 molecules produced per molecule of NO_x before the NO_x is oxidized to more stable products, i.e., NO_z species (Trainer et al., 1993; Wang et al., 2017). Smaller values of OPE indicate the inefficiency of the "NO_x cycle" (Fig. A1), suggesting that the supply of RO_2 from VOC becomes the limiting factor. As a result, the photochemical system tends to be VOC-limited. Conversely, when OPE values are higher, the system tends to be NO_x-limited. Additionally, several modifications had been made to the OPE indicator to account for different situations, such as replacing ΔO_3 with ΔO_x (O_x=O_3+NO_2) (Kleinman et al., 2002) and replacing ΔNO_z with ΔNO_y (NO_y=NO_z+NO_x) (Wang et al., 2006). Other chemical species have also been utilized as photochemical indicators, including the ratio of H_2O_2 to HNO_3 (Hammer et al., 2002). High values of $\frac{H_2O_2}{HNO_3}$ indicate high potential for cross-reactions of two HO_2 radicals, which is associated with high $\frac{VOC}{NO_x}$ and thus indicative of the NO_x-limited regime. For a more widespread application, space-based $\frac{HCHO}{NO_2}$ measurements from global O_3 monitoring satellites have been introduced as an indicator (Martin et al., 2004), based on the fact that levels of HCHO and NO_2 in the tropospheric column are closely linked to VOC and NO_x emissions, respectively. However, all these indicators are not inherently linked to the O_3 formation process, and the corresponding threshold values depend on environmental conditions (Liu and Shi, 2021). This makes it challenging to universally apply these indicators.

During the past decade, highly oxygenated organic molecules (HOM) have been recognized as a new group of VOC oxidation products, particularly important for the formation of secondary organic aerosol (SOA) due to their fast formation and low volatilities (Ehn et al., 2014; Bianchi et al., 2019). Aerosols play a significant role in both impacting human health adversely (Kelly and Fussell, 2015) and influencing climate (Boucher et al., 2013). Formed in the atmosphere-mimicking gas

phase and containing six or more oxygen atoms (Bianchi et al., 2019), HOM are produced via RO_2 autoxidation which rapidly increases their oxygen content through intramolecular H atom abstractions followed by O_2 additions (Crounse et al., 2013; Ehn et al., 2014). Eventually, these highly oxygenated RO_2 will generally be terminated similarly as other RO_2, such as through bimolecular reactions with NO_x, RO_2 or HO_2 radicals (i.e., R4, R5 and R6).

$$RO_2 + RO_2 \rightarrow ROOR + O_2 \quad \text{R5a}$$

$$\rightarrow ROH + RC{=}O + O_2 \quad \text{R5b}$$

$$RO_2 + HO_2 \rightarrow ROOH + O_2 \quad \text{R6a}$$

$$\rightarrow RC{=}O + H_2O + O_2 \quad \text{R6b}$$

The O_3 formation precursors, namely NO_x and VOC, thus are intrinsically connected also to HOM formation through RO_2 chemistry. As such, if the daytime HOM distribution is dominated by organic nitrates, it suggests that the majority of RO_2 are being terminated by reactions with NO (R4), thus contributing to O_3 formation. On the other hand, if we observe large amounts of HOM dimers or non-nitrate monomers, formed from RO_2 + RO_2/HO_2 (R5 and R6), there must be a large fraction of RO_2 that do not contribute to the O_3 formation process, suggesting that increased NO_x would also lead to more O_3. In other words, ratios of different types of HOM can function as another indicator for determining the sensitivity of O_3 formation. The situation is complicated by several factors, including challenges in identifying which HOM might have formed from RO_2 termination by RO_2 or HO_2, or by knowing if a HOM is a monomeric product of a larger VOC precursor or a dimeric product from smaller VOC. Still, if HOM could be used even as a qualitative indicator for O_3 formation, one particular benefit would be that they would serve as a real-time indicator. This is because both the formation (through autoxidation) and loss (through condensation onto aerosol particles) of HOM take place on timescales of minutes or less.

In this study, our objective is to assess the viability of using the ratio of HOM dimers or non-nitrate monomers to HOM organic nitrates as an indicator of O_3 formation sensitivity. We conducted a series of experiments in an atmosphere simulation chamber (Riva et al., 2019a), focusing on the ozonolysis of α-pinene, the most abundantly emitted monoterpene (Pathak et al., 2007). By varying the concentrations of O_3 formation precursors NO_x and α-pinene, as well as the NO_2 photolysis rate, we explored the shift between NO_x-limited and VOC-limited regimes in the chemical system. We employed mass spectrometers and gas monitors to measure HOM products, α-pinene, O_3, and NO_x. We also developed a simple 0-D box model to simulate the concentrations of O_3 and its precursors in the chamber under different conditions. Finally, by analyzing both experimental and model outcomes, we evaluated the potential of the HOM ratios as indicators of O_3 formation sensitivity (either ~~VOC-limited~~ VOC- or NO_x-limited) in this system.

2 Methods

2.1 Experiments

The experiments were conducted in the COALA chamber, as presented by Riva et al. (2019a). The cuboid chamber is made of fluorinated ethylene propylene (FEP) and has a volume of 2 m^3 with a volume to surface area ratio of 0.2. The chamber was run in "steady-state mode" (Peräkylä et al., 2020; Krechmer et al., 2020), meaning there was a continuous flow of air and reagents (O_3, NO_2, and α-pinene) through the chamber. The total flow was around 55 L min^{-1}, giving an average residence time of approximately 36 minutes ($\tau = \frac{2000\ \mathrm{L}}{55\ \mathrm{L\ min^{-1}}} \approx 36\ \mathrm{min}$). Each stage, where the experimental conditions remain unchanged, lasted at least 1.5 hours, which is approximately three times the residence time, allowing the chamber to reach a pseudo steady state, as confirmed by the time series obtained during the experiments (e.g., Fig. 4).

Table 1. Experimental conditions. Each experiment consisted of ~~3-9~~ 3–9 "stages" that corresponded to a specific time period during which the inputs remain constant. The parameter that was varied included input O_3, α-pinene, or NO_x concentrations, as well as NO_2 photolysis rate (J_{NO_2}). These variations are indicated in the table by multiple values or ranges in a given cell. Experiment numbers (No.) and number of total stages per experiment are shown in the first two columns.

		Input			
Experiment *No.*	Number of stages	J_{NO_2} (s^{-1})	O_3 (ppb)	α-pinene (ppb)	NO_x range (ppb)
1.	7	1.85×10^{-3}	10.5	30/60	0 –~ 21.5
2.	8	1.85×10^{-3}	15	15/45/60	0 –~ 21.5
3.	9	1.85×10^{-3}	22.5	10/45/60	0 –~ 35.2
4.	9	1.15×10^{-3}	15.5	15/45/60	0 –~ 44.5
5.	9	0.35×10^{-3}	15.5	15/45/60	0 –~ 44.5
6.	3	1.85×10^{-3}	10/15.5/22.5	60	44.5
7.	8	1.85×10^{-3}	10	30/45/60	0 –~ 21.5

The details of the conducted experiments are provided in Table 1. The UV LED lights (wavelength $\sim$ 400 nm, manufactured by LEDlightmake Inc., Shenzhen, China) (Zhao et al., 2023a) used for photolyzing NO_2 were kept on throughout each experiment, while the input concentrations of the precursors NO_2, O_3, and α-pinene were varied across experiments and stages to map out a wide range of different conditions. The photolysis rate was varied by using varying numbers of LED light strips (1, 3, or 5). Experiments without VOC addition (no. ~~Z1-Z5~~Z1–Z5, Table A1) were used to evaluate the photolysis rates (given in Table 1) for each number of light strips. We acknowledge that using alkene ozonolysis for this type of study is not ideal as O_3 also reacts with the VOC, making the determination of actual O_3 formation more complicated. The choice of this system was partly due to our chamber not having ~~a good~~ the optimal light source for producing OH radicals, thus limiting us to O_3 oxidation, and partly because the HOM spectra from this system has been studied in great detail, making the interpretation of the HOM easier.

All the input reactants, as well as the HOM products, were continuously measured online using instruments described below. The identified HOM species in this study were categorized into three groups: 1) "HOM monomers" (HOM_{Mono}), C_8-C_{10} compounds without any nitrogen atoms; 2) "HOM organic nitrates" (HOM_{ON}), C_8-C_{10} compounds with one nitrogen atom; and 3) "HOM dimers" (HOM_{Di}), C_{18}-C_{20} compounds without any nitrogen atoms.

2.2 Instrumentation

2.2.1 Mass spectrometers

A nitrate-adduct Chemical Ionization Mass Spectrometer (NO_3-CIMS, Tofwerk AG/Aerodyne Research, Inc.) was used for online measurements of HOM with high selectivity (Jokinen et al., 2012; Ehn et al., 2014; Riva et al., 2019b). A large sheath flow of 20 L min^{-1} (to minimize wall losses) carries nitric acid (HNO_3) across X-rays, producing nitrate ions (NO_3^-). Then, in an electric field, NO_3^- are guided towards a 10 L min^{-1} sample flow, ionizing targeted HOM molecules by clustering with them (Kürten et al., 2014). Finally, the charged sample molecules are directed through a critical orifice and into an Atmospheric Pressure Interface Time-of-Flight Mass Spectrometer (APi-TOF), where they are detected based on mass-to-charge ratios (m/z) (Junninen et al., 2010). The NO_3-CIMS was equipped with a standard TOF (HTOF), having a mass resolution of 5000 at m/z 188 Th. The concentrations of HOM were converted from their normalized signals (i.e., the ratio of HOM-containing ions to reagent ions) by multiplying with a calibration factor (C), which takes different efficiencies into account (Jokinen et al., 2012; Bianchi et al., 2019):

$$[HOM] = C \cdot \frac{HOM(NO_3^-)}{\sum_{i=0}^{2}(HNO_3)_i(NO_3^-)} \quad (1)$$

Calibrating with sulfuric acid (Kürten et al., 2012), we determined C to be 1.56×10^9 cm^{-3} ($\pm$50%) based on a flow-tube model (He et al., 2023). However, in this study, the accuracy of C is less important since the normalized signals of HOM were sufficient for relative comparisons.

A Proton Transfer Reaction Time-of-Flight mass spectrometer (PTR-TOF 8000, Ionicon Analytik GmbH), designed for online measurements of VOC (Jordan et al., 2009), was utilized in our study specifically for the detection of α-pinene. The PTR is an ionization method where water molecules (H_2O) are ionized in a hollow cathode discharge, resulting in the formation of hydronium ions (H_3O^+) (Hansel et al., 1995). Then, as proton donors, H_3O^+ are directed into a drift tube, where trace organic compounds are ionized by proton transfer process with proton affinity as the key parameter (Hansel et al., 1995; Graus et al., 2010). After a differentially pumped ion transfer unit, the charged molecules enter a TOF, where collisions are negligible under a low pressure of $\sim 10^{-6}$ mbar with a high vacuum (Graus et al., 2010). The inlet flow was 1 L min^{-1} with 0.1 L min^{-1} being sampled into the ion drift tube. Further details regarding the calibration and settings of the PTR can be found in Zhao et al. (2023b), and the calibration factor for α-pinene (detected as $C_{10}H_{17}^+$ at m/z 137 Th) was $\sim$104 ppb^{-1} after normalization by primary ion isotope $H_3{}^{18}O^+$ (at 21 Th). The analysis of raw data from the NO_3-CIMS and PTR-TOF was conducted using the MATLAB-based set of programs called tofTools (version 611) (Junninen et al., 2010).

2.2.2 Gas monitors

The concentrations of NO_x and O_3 were measured by gas monitors. A photometric O_3 analyzer - model 400 (Teledyne API) was used to detect O_3 in the chamber. The amount of O_3 determines how much of a 254 nm UV light signal is absorbed in the sample cell. The absorption difference between the intact sample air and the O_3-removed air, achieved by a switching valve periodically, enables the determination of the stable O_3 concentrations.

As for NO_x, a NO-NO_2 analyzer - model T200UP (Teledyne API) was utilized. With a high-efficiency photolytic converter, NO_2 is transformed to NO with minimal interference from other gases. Using the chemiluminescence detection principle, NO is measured by reacting with O_3, yielding light in direct proportion to the amount of NO (Archer et al., 1995). In this way, both sampled NO and total NO_x can be measured, without and with using the photolytic converter, respectively. This enables the determination of the NO_2 concentration in the sample by subtraction.

2.3 Box model

As O_3 was both injected and produced in the chamber, and sinks included reactions with NO and VOC as well as flush out, we constructed a simple 0-D box model (~~12 reactions, 9 species,~~ 14 reactions, Table A2) to mimic the main reactions and to generate O_3 isopleth diagrams. These isopleths were then used to determine sensitivity regimes for O_3 formation. Reaction rates were adapted from the NIST Chemical Kinetics Database (https://kinetics.nist.gov/kinetics/index.jsp). The model did not include closed-shell HOM products and all peroxy radicals were treated as a single term (i.e., "RO_2"). The box model was first employed to determine NO_2 photolysis rates under different numbers of UV lights in the zero-VOC experiments (Table A1), where only O_3 and NO_2 were used as input species. The high agreement between model and observation (detailed results are shown in section 3.1 and 3.3) showed that the model was adequate for simulating the targeted reactions in our chamber.

3 Results and discussions

3.1 NO_2 photolysis rate determination

Figure 1 illustrates an example of a zero-VOC experiment, while Table A1 provides a comprehensive list of all zero-VOC experiments conducted. Using the box model, NO_2 photolysis rates (J_{NO_2}) were ~~fitted to accurately simulate the gas concentrations, namely~~ determined by varying the J_{NO_2} parameter in the model until the simulated O_3 and NO_x~~, at each stage of the experiment. With a NO_2 photolysis rate of~~ values agreed with the observations in the zero-VOC experiments (Fig. 1 and A2–A5). With J_{NO_2} = 1.85×10^{-3} s^{-1} with 5 UV lights, the modeled gas concentrations agreed extremely well with measured values (Fig. 1). Similar agreement was observed for different inputs of O_3 and NO_2 (Fig. A2 and A3), indicating the robustness of both ~~model and~~ the model itself and the fitted J_{NO_2}. Furthermore, employing the same procedure, the photolysis rates with 3 and 1 UV lights were determined to be 1.15×10^{-3} s^{-1} and 0.35×10^{-3} s^{-1}, respectively (Fig. A4 and A5). The values for J_{NO_2} could also be computed from the observed steady-state and input concentrations of NO_x/O_3 for each condition (details see Table A1).

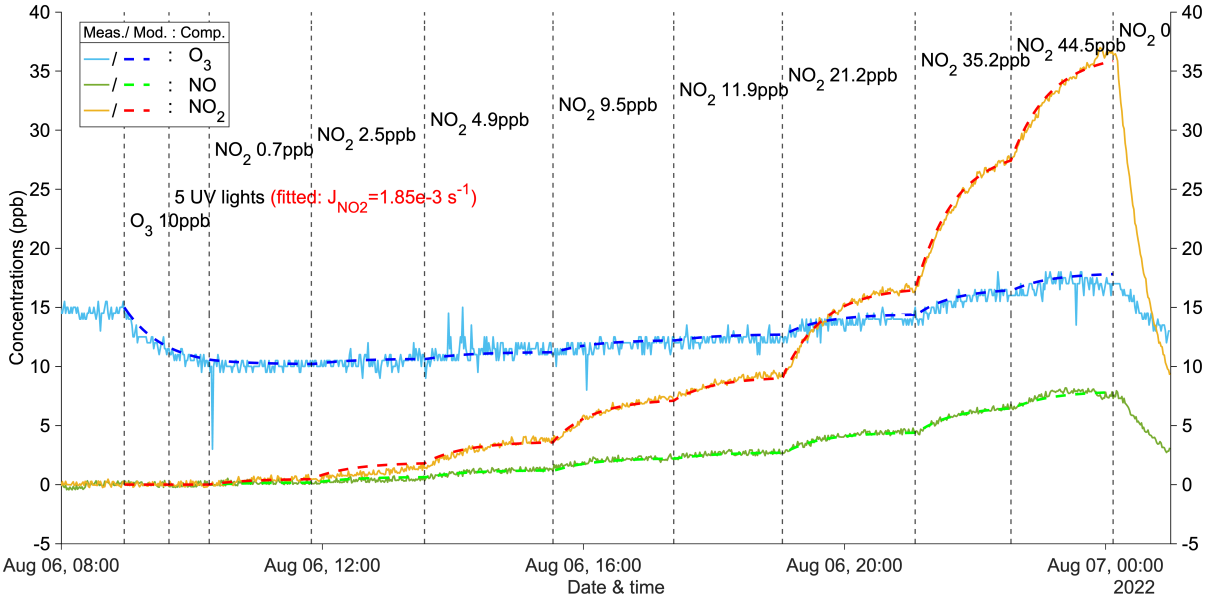

Figure 1. A zero-VOC experiment (Z1) for determining the photolysis rate of NO_2. Measured (abbreviated as Meas.) and modeled (abbreviated as Mod.) concentrations of different compounds (abbreviated as Comp.) are shown in solid and dashed lines respectively. Dashed vertical lines indicate specific time points of operations, with corresponding labels for each operation. Note that the operation labels show input information (input NO_2 = measured NO_2 + NO).

3.2 HOM determination

A steady-state spectrum (experiment no. 2) obtained from the NO_3-CIMS (Fig. 2) illustrates the identified closed-shell HOM products, including HOM_{Mono} (light green), HOM_{ON} (blue), and HOM_{Di} (dark green). Table 2 provides the formulas of all the selected HOM species. Figure A6 displays the steady-state spectra of all stages, with the corresponding input information described in Fig. 4a. As expected, with the injection of more NO_2, the signals of HOM_{ON} increased, while those of HOM_{Mono} and HOM_{Di} decreased considerably (stage (2) –~ (5) in Fig. A6). This observation is consistent with the dominance of the RO_2 + NO reaction over the RO_2 cross-reactions at a few ppb of NO_x (Yan et al., 2016, 2020). After the addition of more α-pinene, all signals showed a noticeable rise (stage (6) –~ (7) in Fig. A6) due to the increased supply of RO_2 species.

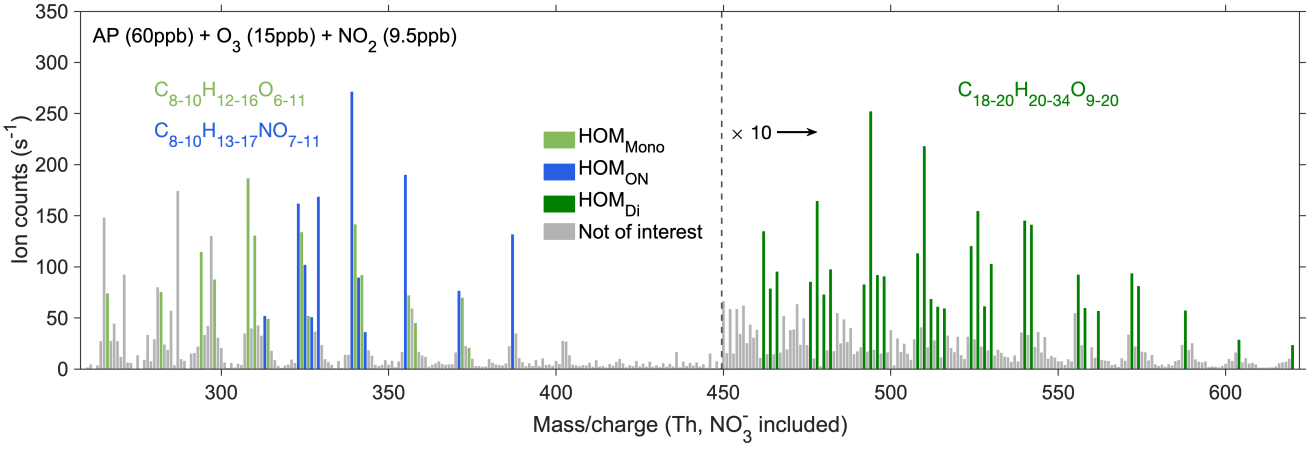

Figure 2. The steady-state spectrum (15 min average) at the stage (7) of experiment no. 2 from the NO_3-CIMS. The spectrum was corrected by subtracting the corresponding background signals. Light green bars show HOM_{Mono}, dark green ones show HOM_{Di}, blue ones show HOM_{ON} while grey ones show peaks not of interest. The peaks not of interest either exhibited relatively low signals, represented radicals, contained too small a number of carbon/oxygen atoms, or had uncertain mass-to-charge ratios. The peaks larger than 450 Th are multiplied by 10.

Our experiments showed that HOM organic nitrates with fewer than 9 oxygen atoms ($HOM_{ON,O\leq8}$) exhibited the slowest decay at the end of the experiment (Fig. 3). This can be explained by the evaporation of these semi-volatile $HOM_{ON,O\leq8}$ compounds from chamber walls even after the gas phase production had stopped. ~~Despite showing a faster decay compared to $HOM_{ON,O\leq8}$~~Additionally, non-nitrate HOM monomers with fewer than 9 oxygen atoms ($HOM_{Mono,O\leq8}$) also showed ~~overall slow decays~~ an overall slow decay (Fig. 3). As a result, prior to subsequent experiments, the concentration levels of $HOM_{ON,O\leq8}$ and $HOM_{Mono,O\leq8}$ remained high, obscuring actual concentration changes following the addition of NO_x. ~~In~~ As such, the ratios of the different compound groups are impacted by memory effects from previous experiments and wall interactions, and would therefore be poor real-time indicators of the O_3 formation sensitivity. In the atmosphere, the long-lived oxygenated VOC (OVOC) could linger for hours to days, and the ratios of e.g., nitrates to non-nitrates would be greatly influenced by various loss terms (photolysis, oxidation, condensation, hydrolysis, etc) that may differ dramatically between different compound

Table 2. Identified HOM closed-shell species based on the experiment no. ~~2~~ 2. The reagent ion NO_3^- is excluded.

Monomers	Dimers	
$C_8H_{12}O_x$ (x=~~6-9~~6–9)	$C_{18}H_{22}O_x$ (x=~~17-20~~17–20)	$C_{19}H_{32}O_x$ (x=~~10-13~~10–13)
$C_{10}H_{14}O_x$ (x=~~7-11~~7–11)	$C_{18}H_{24}O_x$ (x=12,14,16,17)	$C_{20}H_{20}O_{15}$
$C_{10}H_{16}O_x$ (x=~~6-11~~6–11)	$C_{18}H_{26}O_x$ (x=~~11-14~~11–14)	$C_{20}H_{30}O_x$ (x=~~10-18~~10–18)
Organic nitrates	$C_{18}H_{26}O_x$ (x=~~11-14~~11–14)	$C_{20}H_{32}O_x$ (x=9,~~11-15~~11–15)
$C_8H_{13}NO_x$ (x=8,9)	$C_{18}H_{30}O_{13}$	$C_{20}H_{34}O_x$ (x=11,12)
$C_9H_{15}NO_x$ (x=8,9)	$C_{19}H_{26}O_x$ (x=~~10-19~~10–19)	
$C_{10}H_{15}NO_x$ (x=~~7-11~~7–11)	$C_{19}H_{28}O_x$ (x=~~9-16~~9–16)	
$C_{10}H_{17}NO_x$ (x=7,8)	$C_{19}H_{30}O_x$ (x=~~9-13~~9–13)	

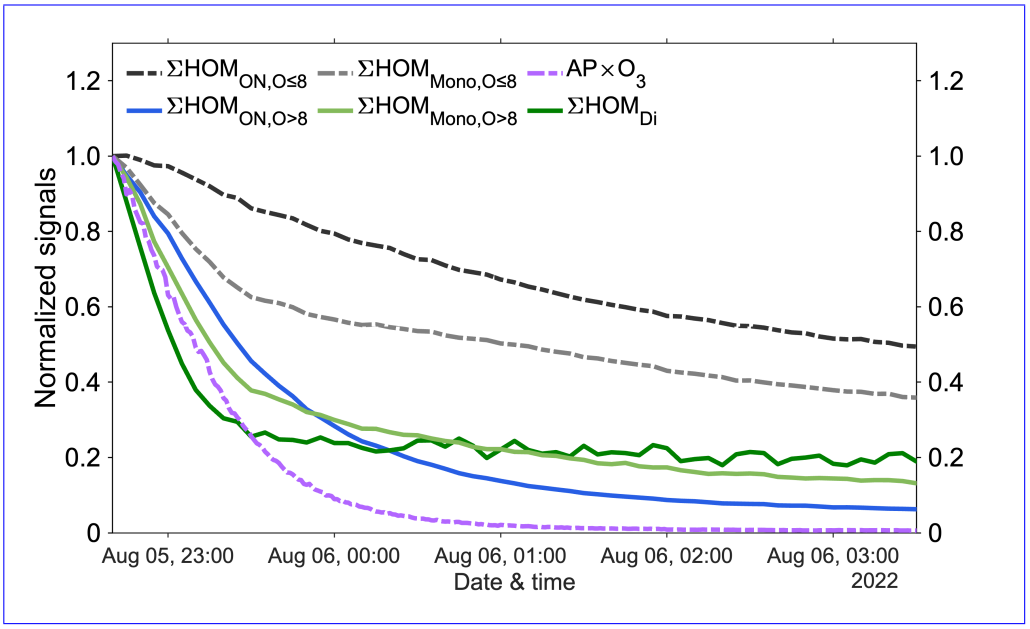

Figure 3. The normalized signal ~~decay of HOM_{ON}, HOM_{Mono}, and HOM_{Di}~~ decays after experiment no. 2 ended. All signals were normalized first to primary ions and then to the signals at the moment when experiment no. 2 ended. Dashed lines: $\sum HOM_{ON,O>8}$ ~~$_{ON,O\leq8}$~~ (sum of HOM_{ON} species with ~~more~~ less than ~~8~~ 9 oxygen atoms~~) are~~ , in ~~solid blue lines~~black), $\sum HOM_{ON,O\leq8}$ ~~are~~ $_{Mono,O\leq8}$ (in ~~dashed black~~ grey), and AP×O_3 (multiplication of α-pinene and O_3 concentrations, in purple). Solid lines: $\sum HOM_{ON,O>8}$ (in blue), $\sum HOM_{Mono,O>8}$ ~~are~~ (in ~~solid~~ light green~~lines~~), and $\sum HOM_{Mono,O\leq8}$ ~~are in dashed grey lines while $\sum HOM_{Di}$ are~~ (in ~~solid~~ dark green~~lines~~).

groups. In contrast, $HOM_{ON,O>8}$, $HOM_{Mono,O>8}$ and HOM_{Di} experienced fast decays ~~, reaching a low and stable level ($\leq$0.2) within a few hours after the experiment~~ (due to their very low volatilities, corresponding to lifetimes well below one hour when

accounting for the fact that HOM formation (roughly estimated by the dashed purple line in Fig. 3) ~~. Despite the~~ continued while the precursors were being flushed out (the higher normalized background level of HOM_{Di} is due to their lower ~~concentrations,~~ initial concentrations, but this stable level allowed for accurate background subtraction in ~~subsequent experiments, enabling measurements of true changes in concentration~~each experiment). Therefore, ~~to ensure the accuracy of our results,~~ we excluded the less oxygenated and more volatile HOM species, specifically $HOM_{ON,O\leq 8}$ and $HOM_{Mono,O\leq 8}$ ~~.~~ to obtain parameters with short enough lifetimes to truly reflect the ongoing chemistry in real-time. The remaining differences in decay rates in Fig. 3 may reflect slight differences in loss rates also for the highly oxygenated species, but also the yields of the different compounds groups are a function of e.g., reaction rates. For example, dimer formation requires RO_2 + RO_2 reactions, which are more favored at higher VOC oxidation rates. Consequently, the indicating ratio used in this study is defined as the ratio between the sum of HOM_{Di} or $HOM_{Mono,O>8}$ and the sum of $HOM_{ON,O>8}$, represented as $\frac{\sum HOM_{Di}}{\sum HOM_{ON,O>8}}$ (Indicating Ratio 1, abbreviated as IR1) or $\frac{\sum HOM_{Mono,O>8}}{\sum HOM_{ON,O>8}}$ (IR2). We emphasize that these ratios will be specific to to our experiments, as yields for the different groups will vary for different VOC and conditions. Nevertheless, the use of the most oxidized, i.e., the least volatile, HOM is critical in this context, as their loss rates are very similar as they all behave as if they were non-volatile, thus condensing irreversibly to surfaces as the main sink term.

3.3 Indicating ratios

In this section, we detail the conducted experiments. Experiment no. 2, is depicted in Fig. 4, while the other experiments are shown in Fig. A7~~–~~–A12. It is worth noting that our experiments did not result in notable particle formation, and condensation to walls was always the dominant loss term for HOM. If aerosol formation had been significant, as has been observed in our chamber at higher oxidation rates (Zhao et al., 2023a), HOM would first increase due to fast formation, and then decrease due to condensation sink. Variation of NO_2 and α-pinene input concentrations lead to changes in both indicating ratios (IR1 and IR2) that correspond with changes in O_3 concentrations (Fig. 4), suggesting a possible sensitivity of O_3 formation. From stage (1) to (5), injection of more NO_2 led to increased formation of $HOM_{ON,O>8}$, while production of HOM_{Di} and $HOM_{Mono,O>8}$ was suppressed. As a result, the indicating ratios decreased. Additionally, the concentration of O_3 increased during this period, but the rate of increase decreased with higher NO_2 inputs. This trend suggests a gradual shift from a NO_x-limited regime to a more VOC-limited regime in the system. For example, during stage (5) with 9.5 ppb NO_2, the O_3 concentration remained relatively constant. This observation indicates the system may have shifted to the VOC-limited regime. Next, when additional α-pinene was introduced ($\sim$ 45 ppb during stage (6)), a significant increase in O_3 concentration was again observed, consistent with the system being in the VOC-limited regime during stage (5). However, after injection of $\sim$ 60 ppb α-pinene during stage (7), the O_3 concentration reached a plateau, indicating that the system had shifted back to the NO_x-limited regime. Moreover, during these two stages, the indicating ratios experienced a substantial increase. In the last stage (8), when additional NO_2 was injected to reach 21.5 ppb, while input α-pinene concentration remained unchanged, the O_3 concentration increased again, and the indicating ratios decreased noticeably, confirming that the previous stage was NO_x-limited. However, it should be noted that the system in this stage might not yet be VOC-limited.

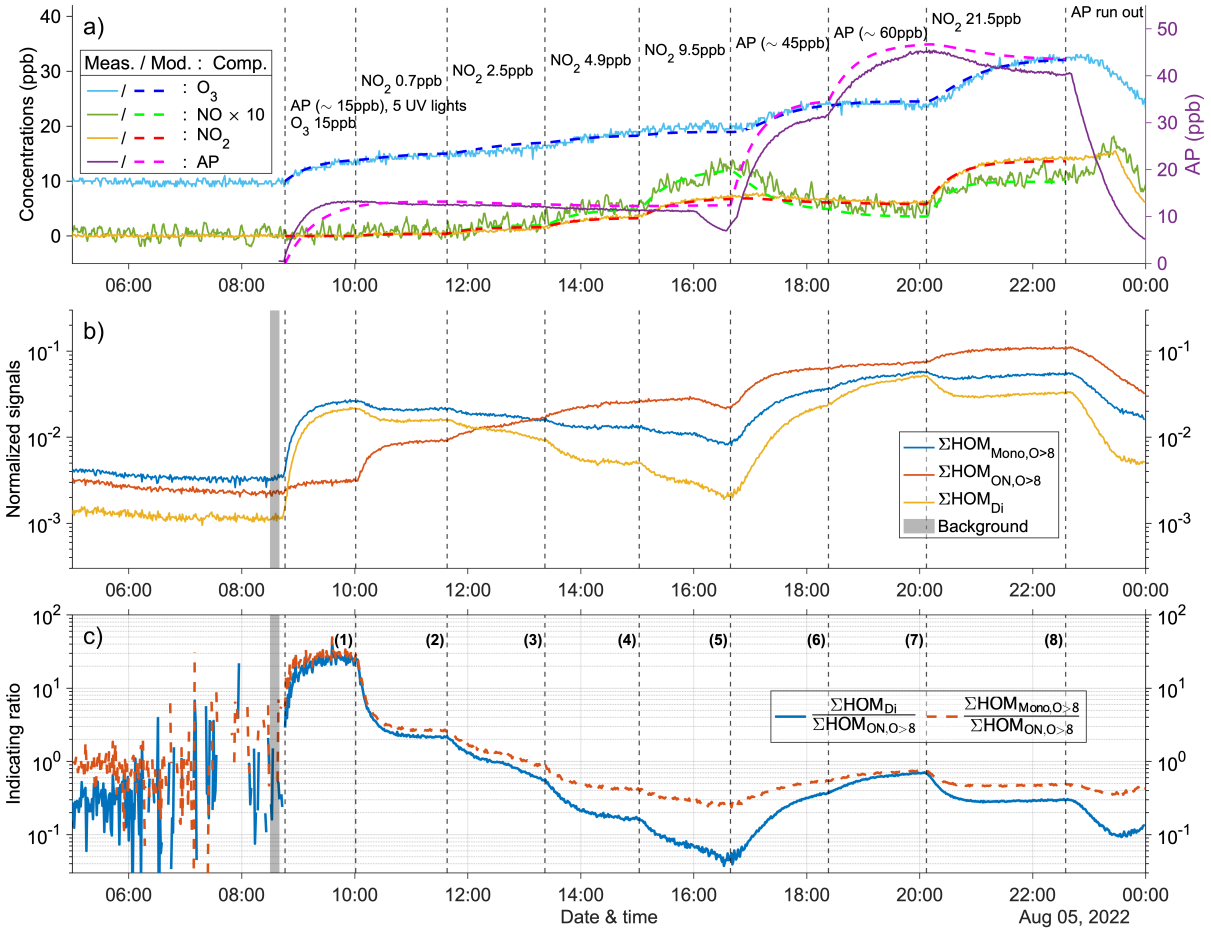

Figure 4. Time series of experiment no. 2 with 15 ppb α-pinene and 15 ppb O_3 as initial inputs. 5 UV lights were on during all stages. Three subplots show the time series of different compounds: a) measured (abbreviated as Meas., in solid lines) and modeled (abbreviated as Mod., in dashed lines) concentrations of O_3, NO_x (both shown by left y-axis; the NO concentration is multiplied by 10), and AP (i.e., α-pinene, shown by right y-axis); b) normalized signals of $\sum HOM_{Mono,O>8}$ (sum of non-nitrate HOM monomers with more than 8 oxygen atoms), $\sum HOM_{ON,O>8}$ (sum of HOM organic nitrates with more than 8 oxygen atoms), and $\sum HOM_{Di}$ (sum of HOM dimers); c) IR1 ($\frac{\sum HOM_{Di}}{\sum HOM_{ON,O>8}}$) and IR2 ($\frac{\sum HOM_{Mono,O>8}}{\sum HOM_{ON,O>8}}$). The grey shaded area represents the time period selected for background subtraction before calculating the ratio. Dashed vertical lines indicate specific time points of operations, with the corresponding labels for each operation in the subplot a. The bolded number in parentheses in subplot c corresponds to the number of stages. The steady-state mass spectra obtained by the NO_3-CIMS for each stage is shown in Fig. A6.

Other experiments with 5 UV lights (Fig. A7, A8, and A11) also exhibited similar time series patterns as described above. One noticeable difference is that higher initial O_3 concentrations resulted in less pronounced increases in O_3 during the first 5 stages with varying NO_2 levels. This can be attributed to the reaction O_3 + NO (R2) becoming faster, competing with the

formation of O_3 from the RO_2 + NO reaction (R4a) followed by NO_2 photolysis (R1). As a result, there was a reduced O_3 formation in the presence of higher initial O_3 concentrations due to the scavenging of NO by existing O_3.

Compared to experiment no. 2 (Fig. 4), experiments with fewer lights (but similar initial concentrations; Fig. A9 and A10) provide insight into the effect of UV light intensities on O_3 formation sensitivity and the consistency of the indicating ratios under different light intensities. More lights led to more pronounced increase in O_3 concentrations at the same stages because additional O_3 was produced from NO_2 photolysis. On the other hand, fewer lights resulted in lower NO levels in the system since NO_2 input was the sole source of NO_x. This led to reduced NO_2 formation from RO_2 + NO reaction (R4a), and subsequently less O_3 formation. This aspect is crucial in determining the O_3 sensitivity. In this sense, the presence of fewer lights implies that higher levels of NO_2 input are required to ensure sufficient NO levels for reaching the VOC-limited regime. This can be confirmed by the stage where $\sim$ 45 ppb α-pinene was injected (Fig. 4, A9, and A10). During this stage, the O_3 concentration showed a significant increase with either 3 or 5 UV lights, indicating that the system had reached the VOC-limited regime in the previous stage. However, when only 1 UV light was used, the O_3 concentration remained relatively constant, suggesting that the system with 1 light did not reach the VOC-limited regime. It is worth mentioning that the indicating ratios exhibited more significant changes when using more lights. This can be attributed to the fact that more lights result in increased production of O_3 and NO, leading to more drastic changes in HOM distributions and thereby influencing the indicating ratios to a greater extent.

Using the box model described in section 2.3, the concentrations of O_3 and its precursors were captured well both qualitatively and quantitatively (e.g., Fig. 4a). In general, simulated concentrations of O_3 during the steady states differed from measured values by at most 10%, while differences for NO_x were even smaller. The largest discrepancy in concentrations ($\sim$ 15%) was observed for α-pinene, which can be attributed to the simplifications made in the model. Specifically, the OH concentration will be underestimated if the model did not accurately capture the yields of HO_2, which can be converted into OH via reactions with NO.

Overall, both indicating ratios are promising as indicators of O_3 formation sensitivity. However, in all time series (Fig. 4c, A7~~e~~ c–A12c), IR1 ($\frac{\sum \mathrm{HOM_{Di}}}{\sum \mathrm{HOM_{ON,O>8}}}$) exhibited more pronounced changes compared to IR2 ($\frac{\sum \mathrm{HOM_{Mono,O>8}}}{\sum \mathrm{HOM_{ON,O>8}}}$) as we shifted the O_3 formation regimes. This highlights that in the well-controlled chamber systems we investigated, IR1 ~~holds~~ may hold better potential for ~~quantitatively~~ indicating O_3 formation sensitivity in the absence of other perturbing factors. It can be explained by the fact that the nitrates are solely from RO_2+NO and the dimers solely from RO_2+RO_2. But HOM monomers can be from both of these reactions. On the other hand, in the real atmosphere, IR1 is expected to be much less robust, as discussed in more detail in section 3.5. The intensity of light (i.e., NO_2 photolysis rate) played a crucial role in determining O_3 sensitivity regimes by controlling the amount of NO. Our box model successfully reproduced the measured values of O_3 and its formation precursors, making it reasonable to extend the model to generate O_3 isopleths under chamber conditions beyond those covered in our experiments. With these we can better elucidate how well the HOM ratios can function as O_3 sensitivity indicators in this system.

3.4 Viability of the indicating ratios

In order to validate the indicating ratio, we generated O_3 isopleths by modeling various combinations of input NO_2 and α-pinene concentrations. The indicating ratios obtained from all steady state stages were scattered on the same coordinate system (IR1: Fig. 5–6 and IR2: Fig. A13–A14). The purpose of varying the injection rates of either NO_x or α-pinene within each experiment (e.g., colored curves in Fig. 5) was to shift the system between the VOC-limited and NO_x-limited regimes. Unlike previous studies that used the concentration of VOC as the x-axis (Kinosian, 1982; Chameides et al., 1992), in this study, the x-axis represented the product of the measured α-pinene and O_3 concentrations. This is because the product reflects the potential for RO_2 formation, which reacts directly with NO to contribute to O_3 accumulation (R1–R4a). In typical EKMA plots the oxidant is primarily thought to be OH, the concentration of which is independent of the VOC concentrations, thus the x-axis would be largely equivalent regardless of whether plotting VOC or VOC times oxidant. In our case, the VOC concentration will directly influence the oxidant (i.e., O_3) concentration through chemical reactions, and therefore we chose to use the current x-axis. The ridge line of the EKMA curves was plotted for each experiment, represented by dotted lines in e.g., Fig. 5b–db–d. The reason for separating the b–d b–d plots from each other is due to the differences in constant O_3 inputs or NO_2 photolysis rates in each experiment, resulting in distinct O_3 isopleths. For the context of this work, we do not separate a transition regime where O_3 formation is sensitive to both NO_x and VOC, but simply define the VOC- and NO_x-limited regimes based on the ridge line. Farther above the ridge line, the system is more VOC-limited, while farther below the line, the system is more NO_x-limited. It's notable that in the VOC-limited regime, instead of a reduction, the O_3 concentration even increased slowly with the addition of NO_x, primarily due to the photolysis of the input NO_2.

Comparing experimental and model results, the steady state stages of all experiments with 5 UV lights exhibited a consistent pattern for the indicating ratios, allowing qualitative determination of O_3 formation sensitivity (Fig. 5 and A13). Generally, the farther the steady state point is from the ridge line, the darker the coloring (either blue or green). Specifically, when the color is darker blue, it indicates a smaller value of the indicating ratios, suggesting a higher likelihood of the system being in the VOC-limited regime. Conversely, when the color is darker green, it signifies a higher value of the ratios, indicating a higher likelihood of the system being in the NO_x-limited regime. It is worth noting that experiment no. 7 was essentially a duplicate of experiment no. 1, but with additional stages. When comparing the indicating ratios at stages with the same inputs, as shown in Fig. 5d and A13d, it becomes apparent that the values are highly consistent and closely aligned. Moreover, the background signals of $HOM_{ON,O>8}$, $HOM_{Mono,O>8}$ and HOM_{Di} increased substantially with experiments going on, from 5×10^{-4} – 2×10^{-3} (Fig. A7b) to 4×10^{-3} – 2×10^{-2} (Fig. A11b). However, the accumulating background did not have a significant impact on the indicating ratios, after the background subtraction (Fig. 5d and A13d). These highlight the remarkable reproducibility of the indicating ratios in our chamber experiments.

To investigate the impact of light intensities, a similar comparison was conducted for experiments with the same initial inputs using 5, 3, and 1 UV lights (Fig. 6 and A14). The observed changes in the pattern of the indicating ratios are in line with those observed in the 5 UV lights experiments described above. The most significant observation is that at lower UV light intensity, the ridge line shifted towards higher NO_x levels at the same potential for RO_2 formation (i.e., the same value of

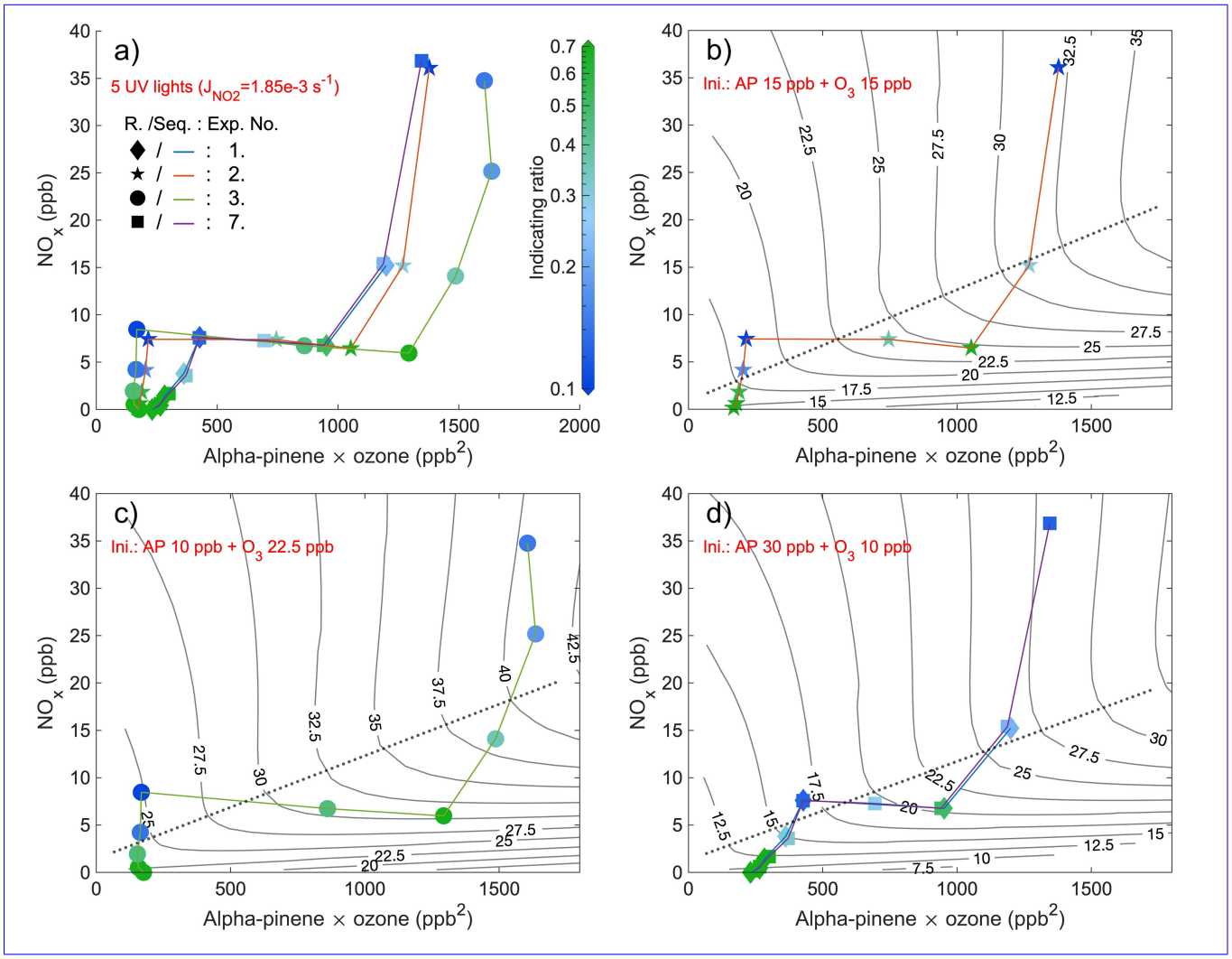

Figure 5. Steady state IR1 ($\frac{\sum \mathrm{HOM_{Di}}}{\sum \mathrm{HOM_{ON,O>8}}}$) of experiments from four days with 5 UV lights. X-axis is the multiplication of ~~measured (~~steady state ~~)~~ α-pinene and O_3 concentrations, while y-axis is the ~~measured (~~steady state ~~)~~ NO_x. The scatter points (exp. no. 1 (experiment number 1): diamond; exp. no. 2: star; exp. no. 3: round; exp. no. 7: square) are colored by values of IR1 (abbreviated as R. in the figure), and are connected by curves (exp. no. 1: blue; exp. no. 2: orange; exp. no. 3: green; exp. no. 7: purple) showing the sequence (Seq.) of experimental stages. Panel a combines stages of all four days, and the rest three subplots respectively show the stages of experiments with different initial (Ini.) inputs (exp. no. 1 and 7 are in the same panel d due to same initial inputs). EKMA curves (isopleth of O_3 concentrations in ppb), simulated by the box model, are black solid lines, while dotted lines are corresponding ridge lines.

x-axis) (Fig. 6~~b–d and A14b–d~~b–d and A14b–d). This finding aligns with the time-series comparison presented in section 3.3, which indicates that at weaker UV intensity, higher input NO_2 is required to generate NO levels sufficient to shift the system towards the VOC-limited regime. When comparing stages with the same conditions except different UV lights, we observed

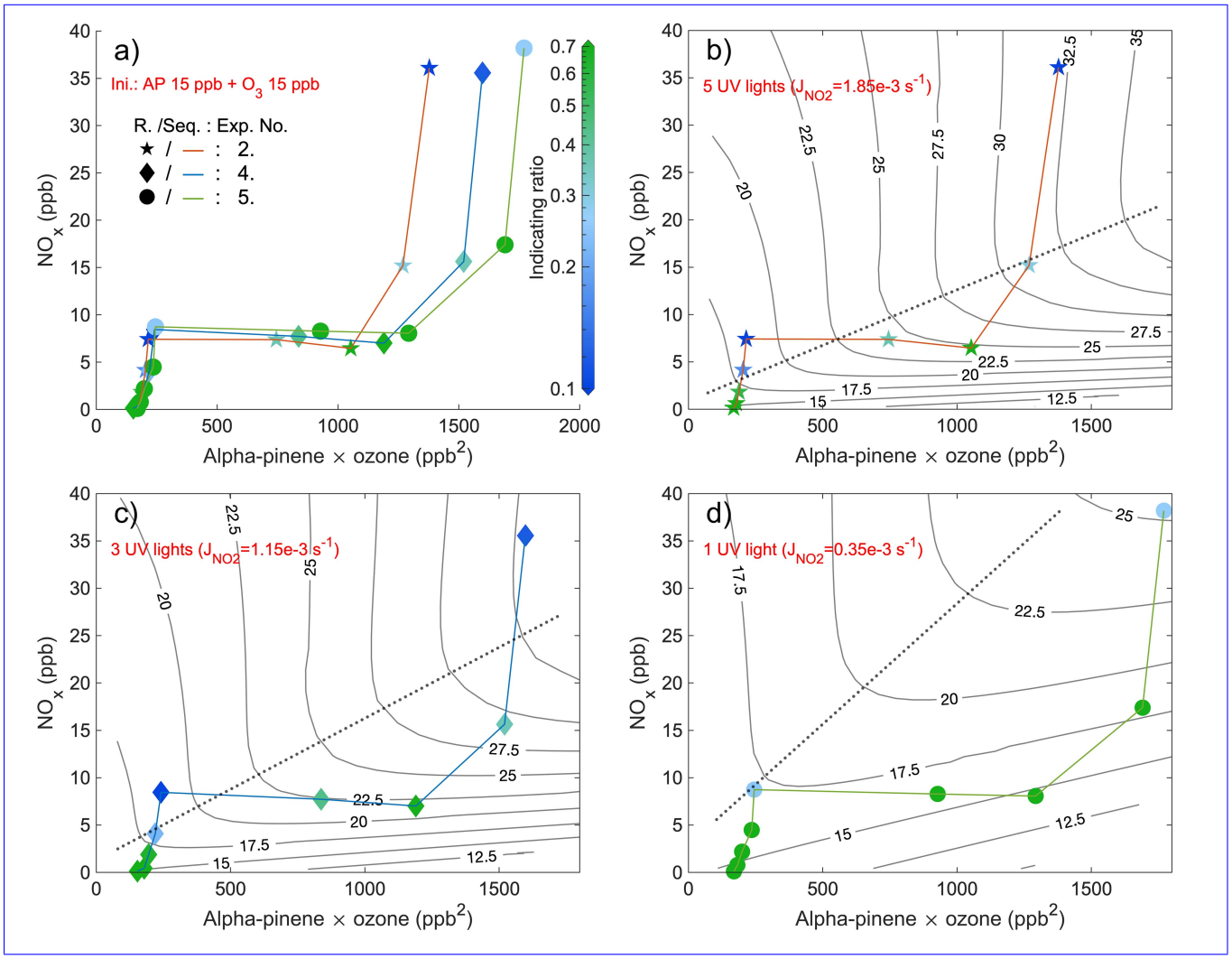

Figure 6. Steady state IR1 ($\frac{\sum \mathrm{HOM_{Di}}}{\sum \mathrm{HOM_{ON,O>8}}}$) of experiments from three days with 5, 3, and 1 UV lights, respectively. X-axis is the multiplication of ~~measured (~~steady state ~~)~~ α-pinene and O_3 concentrations, while y-axis is the ~~measured (~~steady state ~~)~~ NO_x. The scatter points (exp. no. 2 (experiment number 2): star; exp. no. 4: diamond; exp. no. 5: round) are colored by values of IR1 (abbreviated as R. in the figure), and are connected by curves (exp. no. 2: orange; exp. no. 4: blue; exp. no. 5: green) showing the sequence (Seq.) of experimental stages. Panel a combines stages of all three days with the same initial (Ini.) inputs, and the rest three subplots respectively show the stages of experiments with different amount of UV lights. EKMA curves by the box model are in black lines and the dotted lines are corresponding ridge lines.

that generally the lower intensity of UV lights corresponded to higher values of the indicating ratios (Fig. 6 ~~,~~ and A14), showing a higher likelihood of the system being in the NO_x-limited regime. This finding is in agreement with the shift of the ridge line. The correlation between UV intensities, the indicating ratios, and the position of the ridge line reinforces the relationship

between the indicating ratios and O_3 formation sensitivity. It suggests that in addition to the relative changes, the absolute values of the indicating ratios are also informative.

The conclusion can be drawn that the indicating ratios can qualitatively predict the O_3 formation ~~sensitivity, both qualitatively and even quantitatively~~regimes (either VOC- or NO_x-limited). More specifically, based on modeled EKMA curves and steady state HOM ratios (Fig. 5, 6, A13, and A14), regardless of the light intensity, IR1/IR2 consistently indicate the VOC-limited regime when below 0.2/0.4, and the NO_x-limited regime when above 0.5/0.7.

3.5 Implication and further improvements

Our chamber study (section 3.4) confirmed the significant role of the indicating ratios in determining O_3 formation sensitivity ~~, both qualitativelyand quantitatively~~qualitatively. However, in the real atmosphere, the conditions will vary significantly more than in our simple system. Most importantly, the amount of different precursor VOC will be vastly greater, and in reactions with OH, the distribution of different types of RO_2 radicals will also be far more complex. As an example, in a rural setting there can be a wide variety of small VOC (~~C1-C4~~C1–C4), isoprene (C5), aromatics (~~C6-C9~~C6–C9) and monoterpenes (C10) that all produce significant amounts of RO_2. Consequently, from these molecules, dimers can form with any carbon number between 2 and 20, while monomers can have carbon numbers between 1 and 10. In addition, both VOC and oxidant concentrations as well as radiation and meteorological patterns will vary over time. This means that it will be difficult to find universal compounds to include in the HOM_{Di}, HOM_{Mono} and HOM_{ON} groups used to calculate the indicating ratios for a given site and a given time. For example, it is likely that there will be few environments where C10-RO_2 from monoterpenes would be efficiently reacting with each other during daytime, meaning that the C20 dimers used here are unlikely to be usable. It remains to be seen whether the HOM_{Mono}-to-HOM_{ON} ratio can be used for C10 compounds in areas with high monoterpene emissions. Nevertheless, conceptually the link between HOM formation pathways and O_3 formation should hold, and it may be possible to determine suitable compound groups for various sites. Our study focused exclusively on α-pinene, but the intrinsic connection between the indicating ratios we proposed and O_3 formation (Fig. A1) is not limited to this specific VOC. Further laboratory and ambient studies are necessary to investigate additional VOC of interest and expand our understanding of the indicating ratios' applicability and generalizability in predicting O_3 formation sensitivity under various atmospheric conditions. In addition, at the extremes, ranging from clear formation of dimeric species to complete lack of dimeric species with abundant organic HOM nitrates, this can be considered a strong qualitative indicator being in a NO_x- or VOC-limited regime, respectively.

4 Conclusions

Both O_3 and HOM are of significant interest, given their impacts from small-scale personal health to large-scale global climate. Due to the intrinsic connection between the formation mechanisms of O_3 and HOM, we suggest new indicators, denoted as $\frac{\sum HOM_{Di}}{\sum HOM_{ON,O>8}}$ and $\frac{\sum HOM_{Mono,O>8}}{\sum HOM_{ON,O>8}}$, for determining O_3 formation regimes based on the distribution of HOM. One main improvement of using HOM-based indicating ratios compared to those suggested earlier would be the short lifetimes of HOM, which means that these new indicators would be real-time indicators of the formation regime. To assess the viability of the

indicating ratios, a series of chamber experiments were carried out using a NO_3-CIMS, a PTR-TOF, and O_3/NO_x monitors. As expected, an increase in NO_x inputs led to an increase in HOM_{ON} and a decrease in HOM_{Di}, HOM_{Mono} and the indicating ratios. Conversely, an increase in α-pinene resulted in a rise in the indicating ratios. Furthermore, when adding enough of one of the O_3 formation precursors (either NO_x or α-pinene), the rate of increase in O_3 concentration slowed down or even stopped. This indicates that the system was shifting to or had already reached the other limited regime.

With a box model, which closely reproduced the measured concentrations of O_3 and its precursors, O_3 isopleths were obtained for different concentrations of NO_x and α-pinene. After drawing ridge lines of the isopleths, it was observed that the indicating ratios provide a qualitative prediction of the O_3 formation regimes: lower values of the ratios indicate a greater likelihood of the system being located in the VOC-limited regime, and vice versa. With less intense UV light ($\lambda \approx 400$ nm), a higher amount of NO_2 was required to shift the system towards the VOC-limited regime. This can be attributed to a decrease in the formation of NO from NO_2 photolysis. Nevertheless, the absolute values of the indicating ratios exhibited a consistent behavior across different intensities of UV light, suggesting that these absolute values are highly valuable for analyzing O_3 formation sensitivity.

The main objective of this study was to evaluate the concept of using HOM distributions in indicating O_3 formation sensitivity. Based on our outcomes, we can conclude that the ratio of HOM dimers or non-nitrate monomers to HOM organic nitrates (i.e., $\frac{\sum HOM_{Di}}{\sum HOM_{ON,O>8}}$ or $\frac{\sum HOM_{Mono,O>8}}{\sum HOM_{ON,O>8}}$) has the capability to indicate O_3 formation ~~sensitivity, even quantitatively,~~ regimes (either VOC- or NO_x-limited), in this simple system of monoterpene ozonolysis. An indicating ratio of this kind would aid in better control of O_3 pollution and have the potential to be incorporated as a useful parameter in global models for analyzing O_3 formation sensitivity under diverse environmental conditions.

Nevertheless, future studies will need to assess whether this approach is feasible to be applied in real-world conditions where the chemistry is far more complex. The variability of VOC precursors alone will greatly perturb the ideal situation observed in our chamber. Still, we posit that environments with high monoterpene emissions will also produce abundant C10-RO_2 concentrations, and the comparison of the highly oxygenated monomeric termination products (i.e., nitrates vs non-nitrates) can provide an indication of the relative RO_2 termination pathways. Further studies, both ambient observation as well as chamber experiments involving multiple VOC and oxidants, will be necessary to determine the potential of HOM-based indicators for O_3 formation.

Code availability. Code is available upon request from the corresponding authors.

Data availability. Data is available upon request from the corresponding authors.

Appendix A: Additional figures and tables

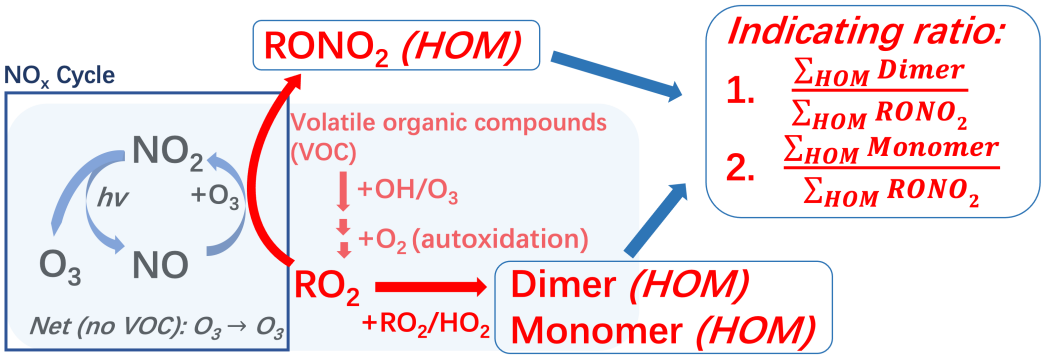

Figure A1. ~~Sketch~~ A sketch of the connection between HOM and O_3 formation. Based on the formation connection, two indicating ratios between the HOM species are defined. "$RONO_2$ *(HOM)*": nitrate-containing HOM monomers, "Dimer *(HOM)*": non-nitrate HOM dimers, "Monomer *(HOM)*": non-nitrate HOM monomers.

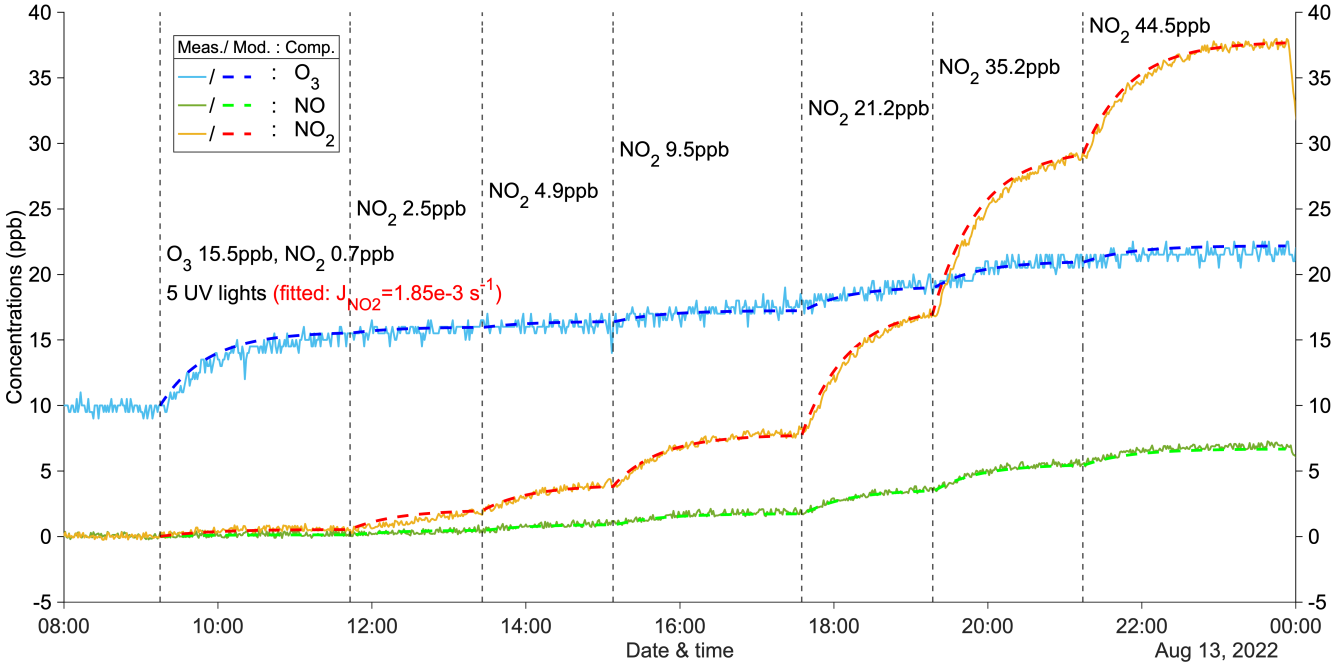

Figure A2. A zero-VOC experiment (Z2) for determining the photolysis rate of NO_2. Measured (abbreviated as Meas.) and modeled (abbreviated as Mod.) concentrations of different compounds (abbreviated as Comp.) are shown in solid and dashed lines respectively. Dashed vertical lines indicate specific time points of operations, with corresponding labels for each operation.

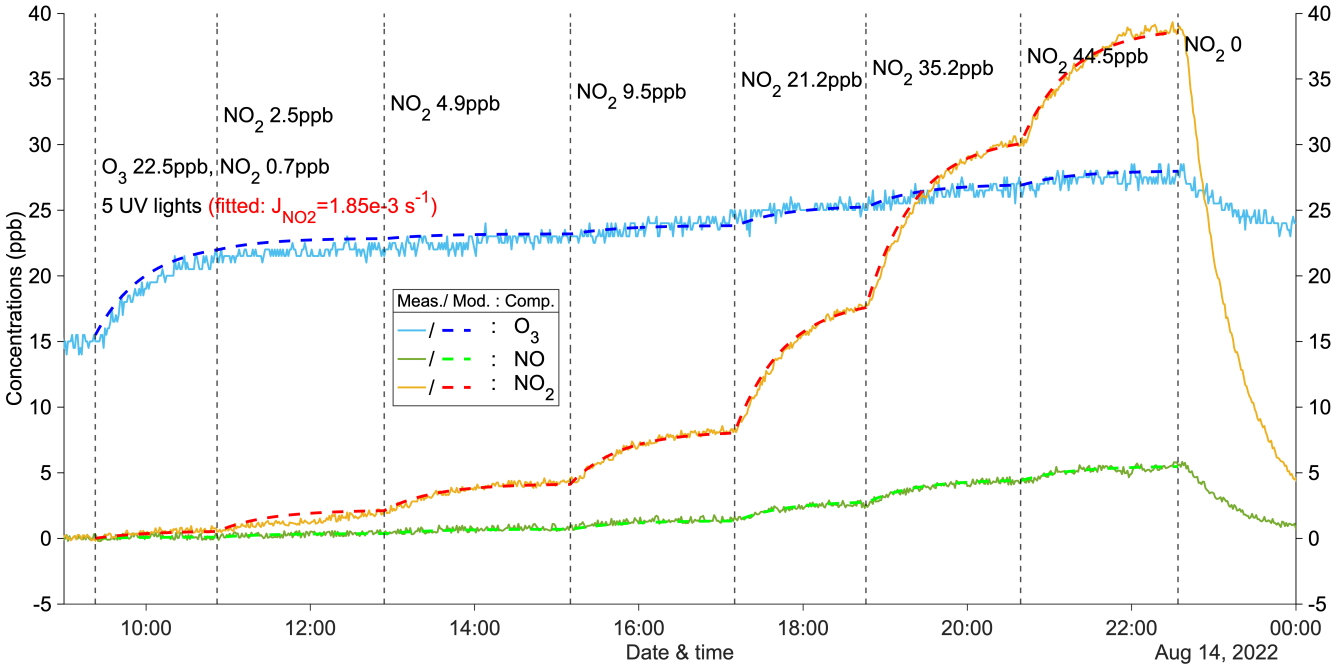

Figure A3. A zero-VOC experiment (Z3) for determining the photolysis rate of NO_2. Measured (abbreviated as Meas.) and modeled (abbreviated as Mod.) concentrations of different compounds (abbreviated as Comp.) are shown in solid and dashed lines respectively. Dashed vertical lines indicate specific time points of operations, with corresponding labels for each operation.

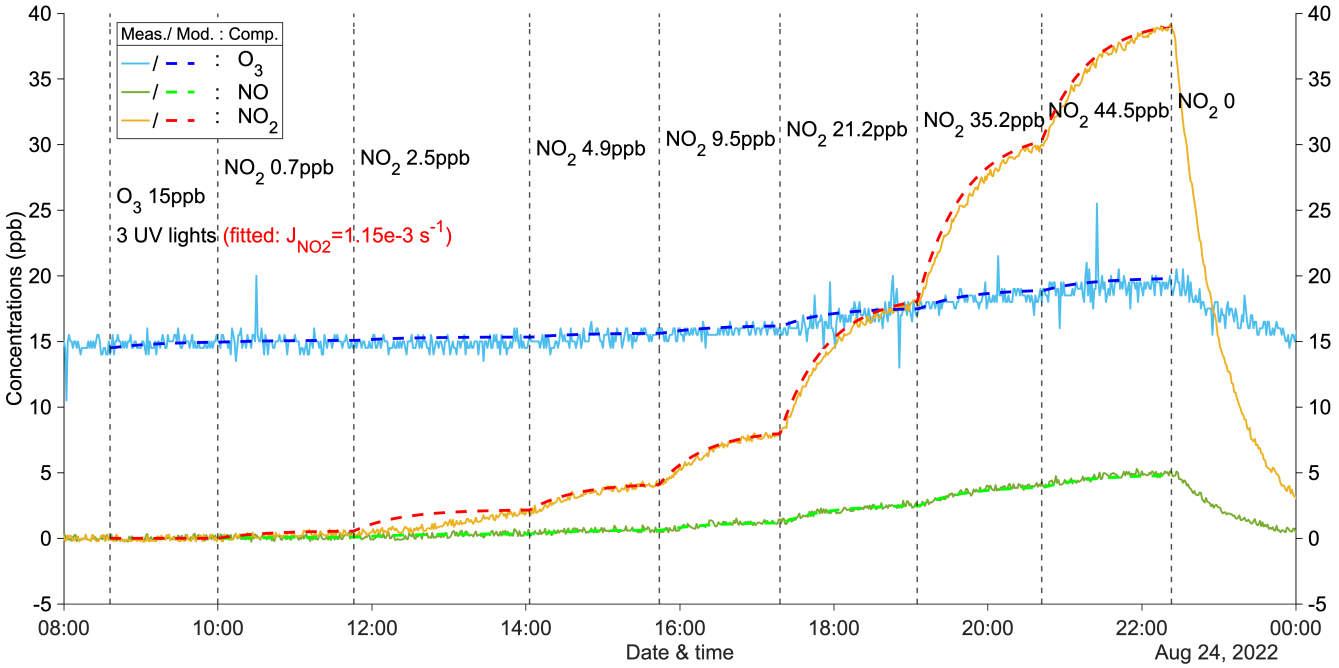

Figure A4. A zero-VOC experiment (Z4) for determining the photolysis rate of NO_2. Measured (abbreviated as Meas.) and modeled (abbreviated as Mod.) concentrations of different compounds (abbreviated as Comp.) are shown in solid and dashed lines respectively. Dashed vertical lines indicate specific time points of operations, with corresponding labels for each operation.

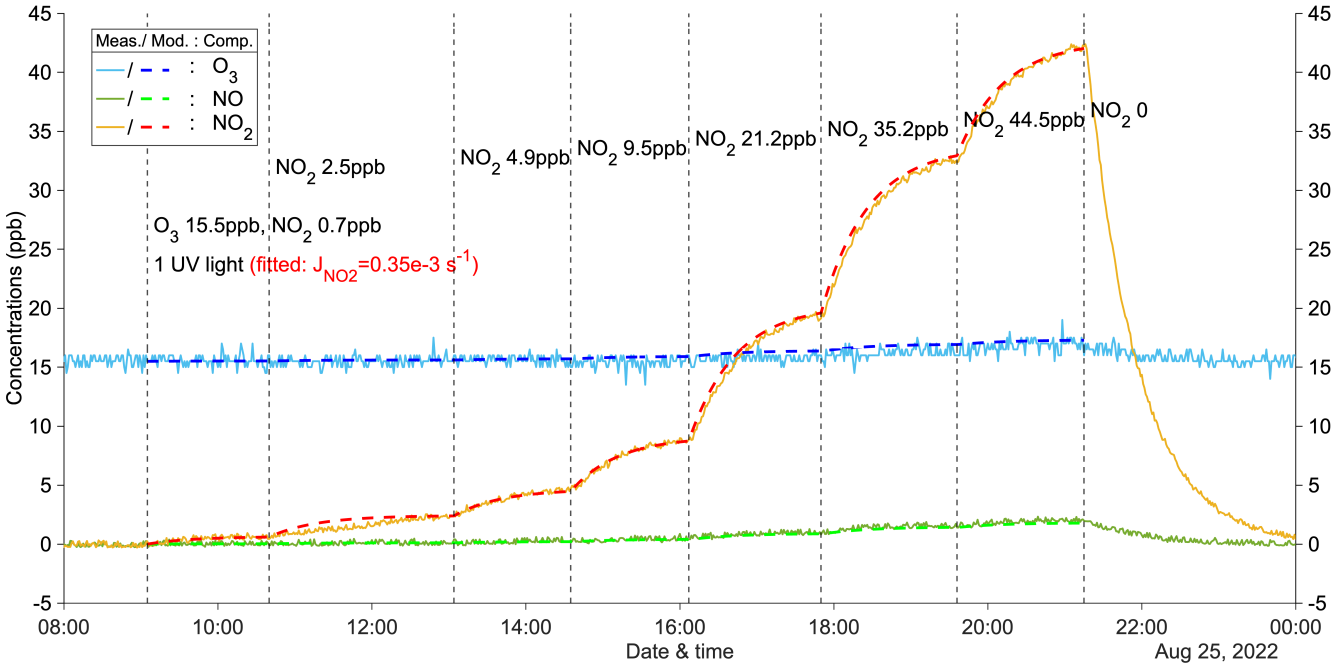

Figure A5. A zero-VOC experiment (Z5) for determining the photolysis rate of NO_2. Measured (abbreviated as Meas.) and modeled (abbreviated as Mod.) concentrations of different compounds (abbreviated as Comp.) are shown in solid and dashed lines respectively. Dashed vertical lines indicate specific time points of operations, with corresponding labels for each operation.

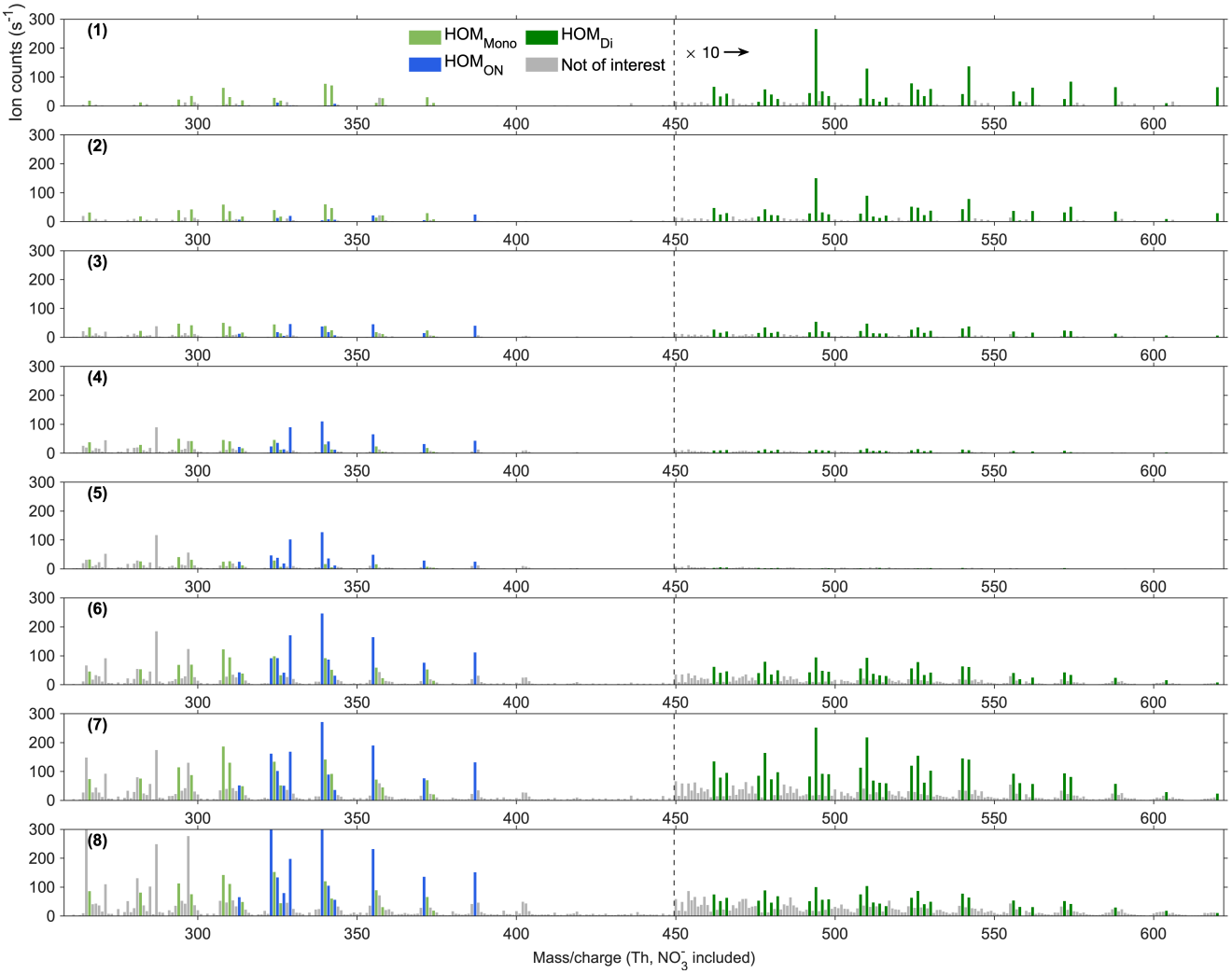

Figure A6. Steady-state spectra (15 min average) at experiment no. 2 from the NO_3-CIMS. All spectra were corrected by subtracting the corresponding background signals. The number at each row show the order of the stage, consistent with the time series in Fig. 4. Light green bars show HOM_{Mono}, dark green ones show HOM_{Di}, blue ones show HOM_{ON} while grey ones show peaks not of interest. The peaks larger than 450 Th are multiplied by 10.

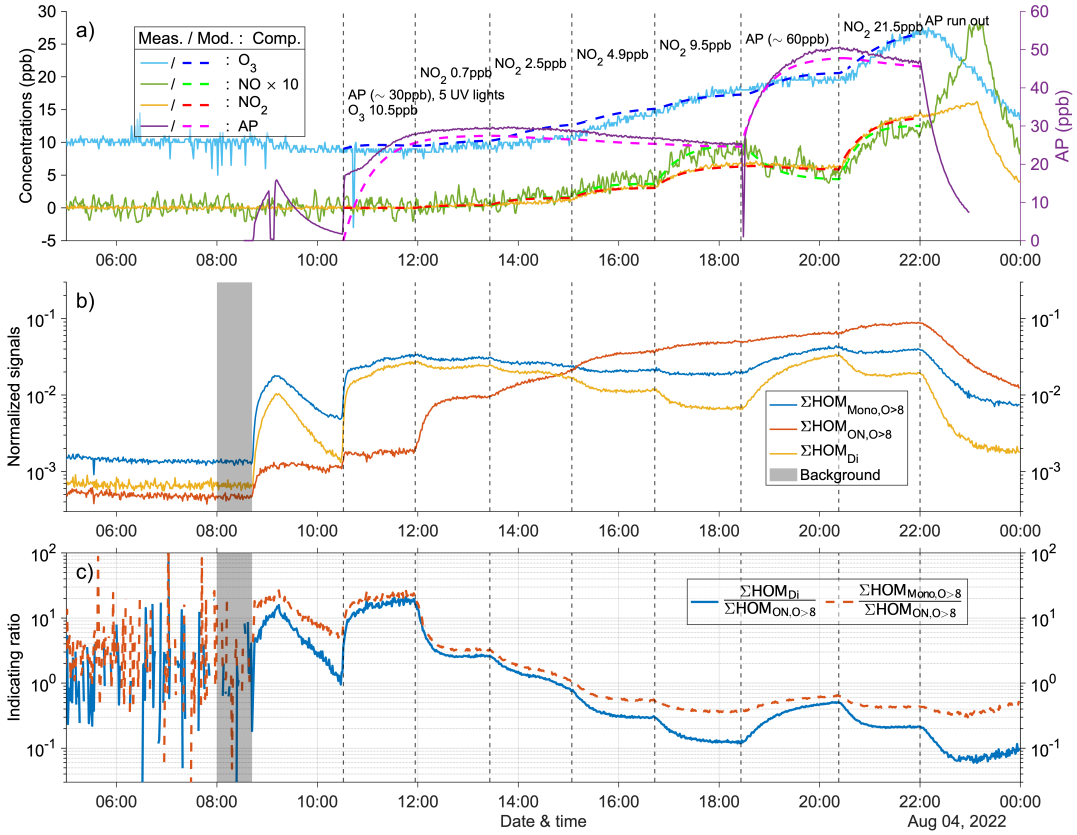

Figure A7. Time series of experiment no. 1 with 30 ppb α-pinene and 10.5 ppb O_3 as initial inputs. 5 UV lights were on during all stages. Three subplots show the time series of different compounds: a) measured (abbreviated as Meas., in solid lines) and modeled (abbreviated as Mod., in dashed lines) concentrations of O_3, NO_x (both shown by left y-axis; the NO concentration is multiplied by 10), and AP (i.e., α-pinene, shown by right y-axis); b) normalized signals of $\sum HOM_{Mono,O>8}$ (sum of non-nitrate HOM monomers with more than 8 oxygen atoms), $\sum HOM_{ON,O>8}$ (sum of HOM organic nitrates with more than 8 oxygen atoms), and $\sum HOM_{Di}$ (sum of HOM dimers); c) IR1 ($\frac{\sum HOM_{Di}}{\sum HOM_{ON,O>8}}$) and IR2 ($\frac{\sum HOM_{Mono,O>8}}{\sum HOM_{ON,O>8}}$). The grey shaded area represents the time period selected for background subtraction before calculating the ratio. Dashed vertical lines indicate specific time points of operations, with the corresponding labels for each operation in the subplot a.

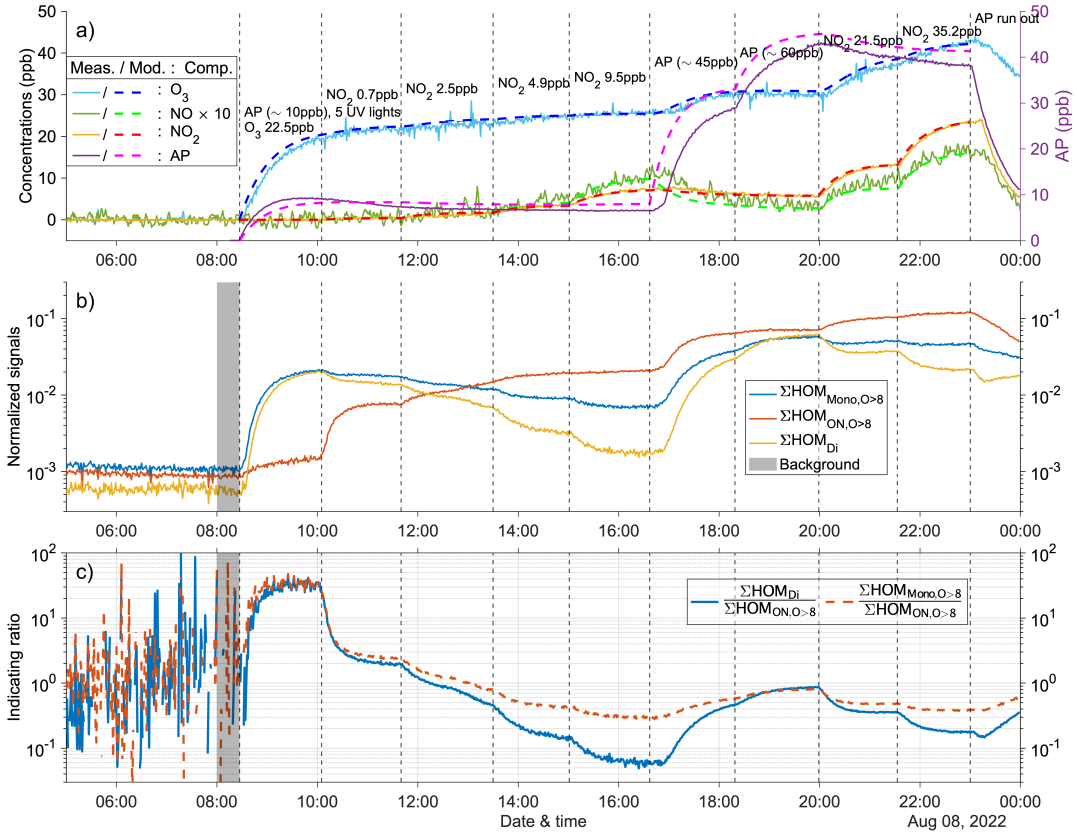

Figure A8. Time series of experiment no. 3 with 10 ppb α-pinene and 22.5 ppb O_3 as initial inputs. 5 UV lights were on during all stages. Three subplots show the time series of different compounds: a) measured (abbreviated as Meas., in solid lines) and modeled (abbreviated as Mod., in dashed lines) concentrations of O_3, NO_x (both shown by left y-axis; the NO concentration is multiplied by 10), and AP (i.e., α-pinene, shown by right y-axis); b) normalized signals of $\sum HOM_{Mono,O>8}$ (sum of non-nitrate HOM monomers with more than 8 oxygen atoms), $\sum HOM_{ON,O>8}$ (sum of HOM organic nitrates with more than 8 oxygen atoms), and $\sum HOM_{Di}$ (sum of HOM dimers); c) IR1 ($\frac{\sum HOM_{Di}}{\sum HOM_{ON,O>8}}$) and IR2 ($\frac{\sum HOM_{Mono,O>8}}{\sum HOM_{ON,O>8}}$). The grey shaded area represents the time period selected for background subtraction before calculating the ratio. Dashed vertical lines indicate specific time points of operations, with the corresponding labels for each operation in the subplot a.

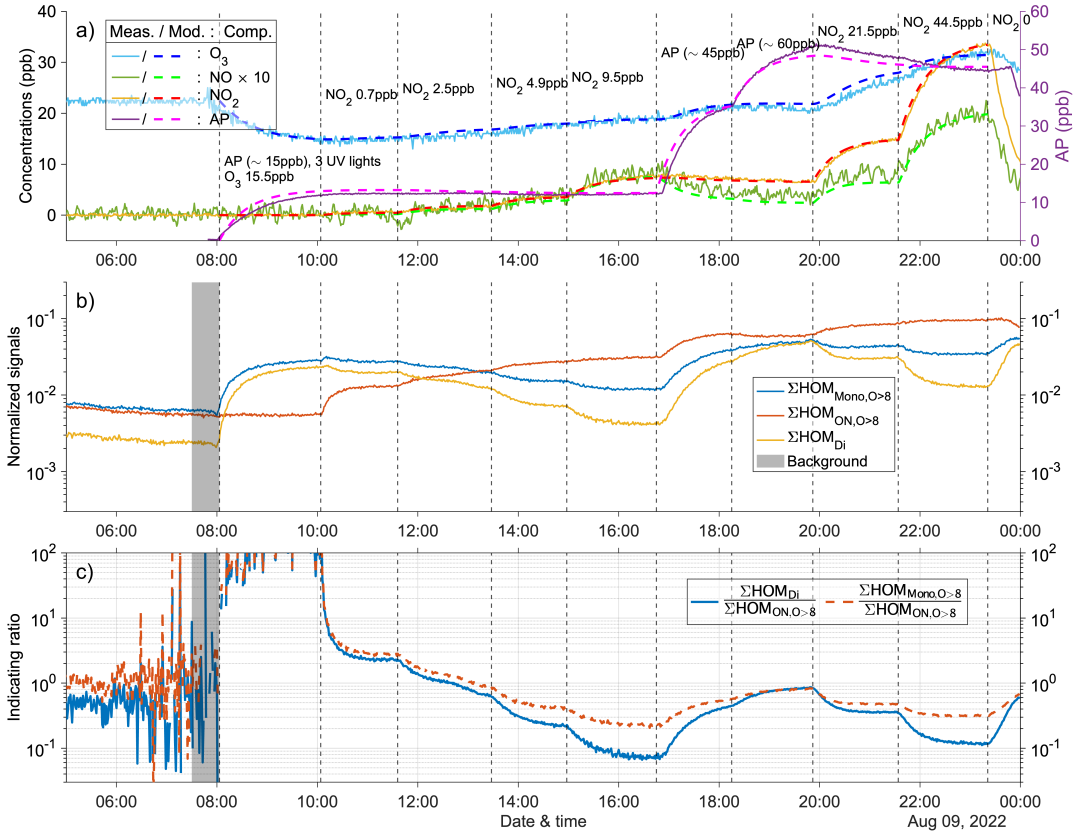

Figure A9. Time series of experiment no. 4 with 15 ppb α-pinene and 15.5 ppb O_3 as initial inputs. 3 UV lights were on during all stages. Three subplots show the time series of different compounds: a) measured (abbreviated as Meas., in solid lines) and modeled (abbreviated as Mod., in dashed lines) concentrations of O_3, NO_x (both shown by left y-axis; the NO concentration is multiplied by 10), and AP (i.e., α-pinene, shown by right y-axis); b) normalized signals of $\sum HOM_{Mono,O>8}$ (sum of non-nitrate HOM monomers with more than 8 oxygen atoms), $\sum HOM_{ON,O>8}$ (sum of HOM organic nitrates with more than 8 oxygen atoms), and $\sum HOM_{Di}$ (sum of HOM dimers); c) IR1 ($\frac{\sum HOM_{Di}}{\sum HOM_{ON,O>8}}$) and IR2 ($\frac{\sum HOM_{Mono,O>8}}{\sum HOM_{ON,O>8}}$). The grey shaded area represents the time period selected for background subtraction before calculating the ratio. Dashed vertical lines indicate specific time points of operations, with the corresponding labels for each operation in the subplot a.

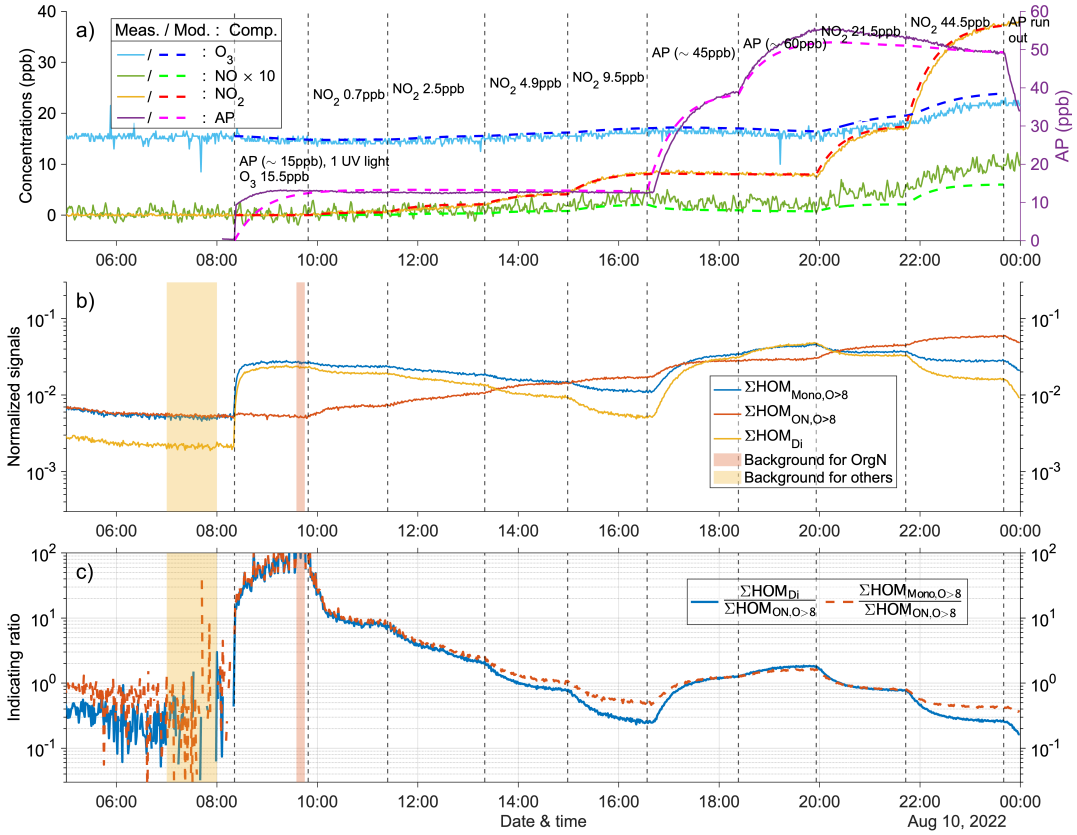

Figure A10. Time series of experiment no. 5 with 15 ppb α-pinene and 15.5 ppb O_3 as initial inputs. 1 UV light was on during all stages. Three subplots show the time series of different compounds: a) measured (abbreviated as Meas., in solid lines) and modeled (abbreviated as Mod., in dashed lines) concentrations of O_3, NO_x (both shown by left y-axis; the NO concentration is multiplied by 10), and AP (i.e., α-pinene, shown by right y-axis); b) normalized signals of $\sum HOM_{Mono,O>8}$ (sum of non-nitrate HOM monomers with more than 8 oxygen atoms), $\sum HOM_{ON,O>8}$ (sum of HOM organic nitrates with more than 8 oxygen atoms), and $\sum HOM_{Di}$ (sum of HOM dimers); c) IR1 ($\frac{\sum HOM_{Di}}{\sum HOM_{ON,O>8}}$) and IR2 ($\frac{\sum HOM_{Mono,O>8}}{\sum HOM_{ON,O>8}}$). The yellow and red shaded area represent the time periods selected for background subtraction of dimers and organic nitrates, before calculating the ratio. Dashed vertical lines indicate specific time points of operations, with the corresponding labels for each operation in the subplot a.

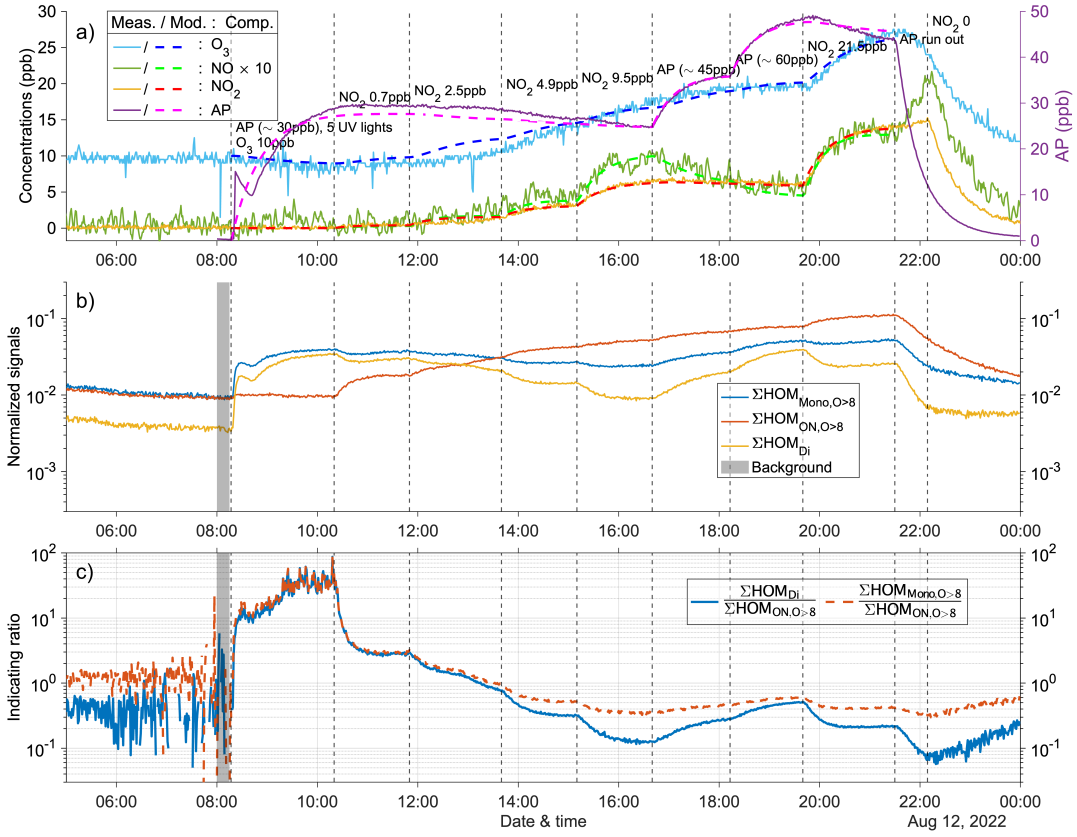

Figure A11. Time series of experiment no. 7 with 30 ppb α-pinene and 10 ppb O_3 as initial inputs. 5 UV lights was on during all stages. Three subplots show the time series of different compounds: a) measured (abbreviated as Meas., in solid lines) and modeled (abbreviated as Mod., in dashed lines) concentrations of O_3, NO_x (both shown by left y-axis; the NO concentration is multiplied by 10), and AP (i.e., α-pinene, shown by right y-axis); b) normalized signals of $\sum HOM_{Mono,O>8}$ (sum of non-nitrate HOM monomers with more than 8 oxygen atoms), $\sum HOM_{ON,O>8}$ (sum of HOM organic nitrates with more than 8 oxygen atoms), and $\sum HOM_{Di}$ (sum of HOM dimers); c) IR1 ($\frac{\sum HOM_{Di}}{\sum HOM_{ON,O>8}}$) and IR2 ($\frac{\sum HOM_{Mono,O>8}}{\sum HOM_{ON,O>8}}$). The grey shaded area represents the time period selected for background subtraction before calculating the ratio. Dashed vertical lines indicate specific time points of operations, with the corresponding labels for each operation in the subplot a.

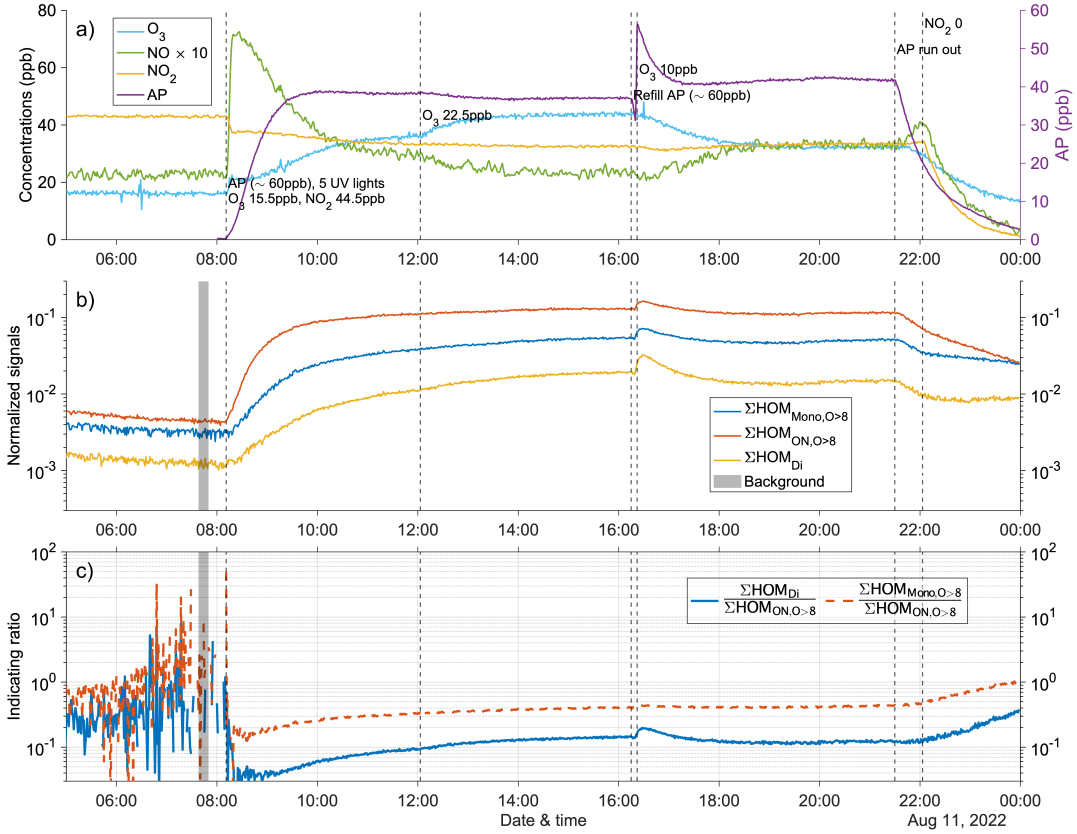

Figure A12. Time series of experiment no. 6, which was meant for collecting more data at the highest NO_2 input (at $\sim$ 44.5 ppb). 5 UV lights was on during all stages. Three subplots show the time series of different compounds: a) measured concentrations of O_3, NO_x (both shown by left y-axis; the NO concentration is multiplied by 10), and AP (i.e., α-pinene, shown by right y-axis); b) normalized signals of $\sum HOM_{Mono,O>8}$ (sum of non-nitrate HOM monomers with more than 8 oxygen atoms), $\sum HOM_{ON,O>8}$ (sum of HOM organic nitrates with more than 8 oxygen atoms), and $\sum HOM_{Di}$ (sum of HOM dimers); c) IR1 ($\frac{\sum HOM_{Di}}{\sum HOM_{ON,O>8}}$) and IR2 ($\frac{\sum HOM_{Mono,O>8}}{\sum HOM_{ON,O>8}}$). The grey shaded area represents the time period selected for background subtraction before calculating the ratio. Dashed vertical lines indicate specific time points of operations, with the corresponding labels for each operation in the subplot a.

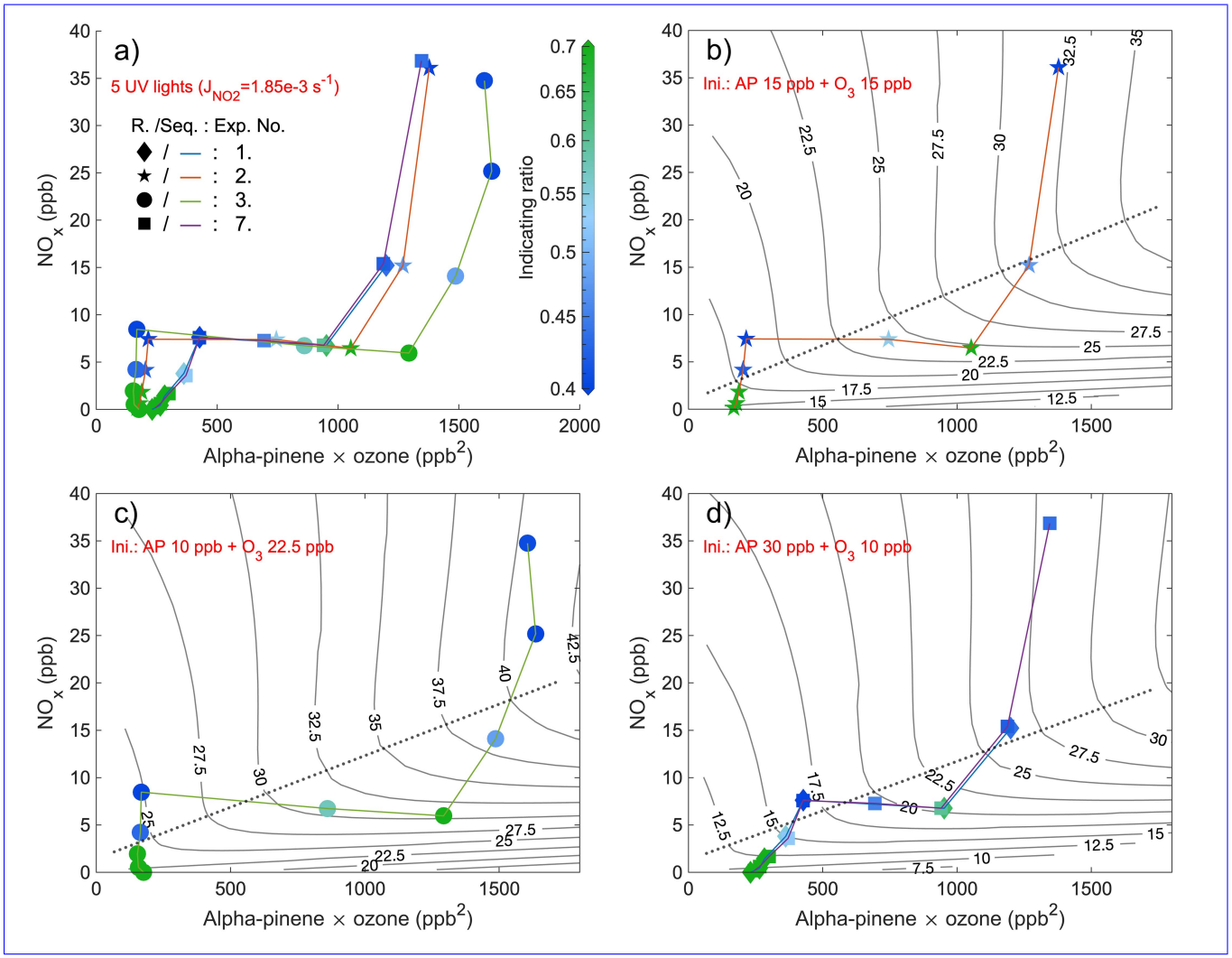

Figure A13. Steady state IR2 ($\frac{\sum \mathrm{HOM_{Mono,O>8}}}{\sum \mathrm{HOM_{ON,O>8}}}$) of experiments from four days with 5 UV lights. X-axis is the multiplication of ~~measured (~~steady state ~~)~~ α-pinene and O_3 concentrations, while y-axis is the ~~measured (~~steady state ~~)~~ NO_x. The scatter points (exp. no. 1 (experiment number 1): diamond; exp. no. 2: star; exp. no. 3: round; exp. no. 7: square) are colored by values of IR2 (abbreviated as R. in the figure), and are connected by curves (exp. no. 1: blue; exp. no. 2: orange; exp. no. 3: green; exp. no. 7: purple) showing the sequence (Seq.) of experimental stages. Panel a combines stages of all four days, and the rest three subplots respectively show the stages of experiments with different initial (Ini.) inputs (exp. no. 1 and 7 are in the same panel d due to same initial inputs). EKMA curves (isopleth of O_3 concentrations in ppb), simulated by the box model, are black solid lines, while dotted lines are corresponding ridge lines.

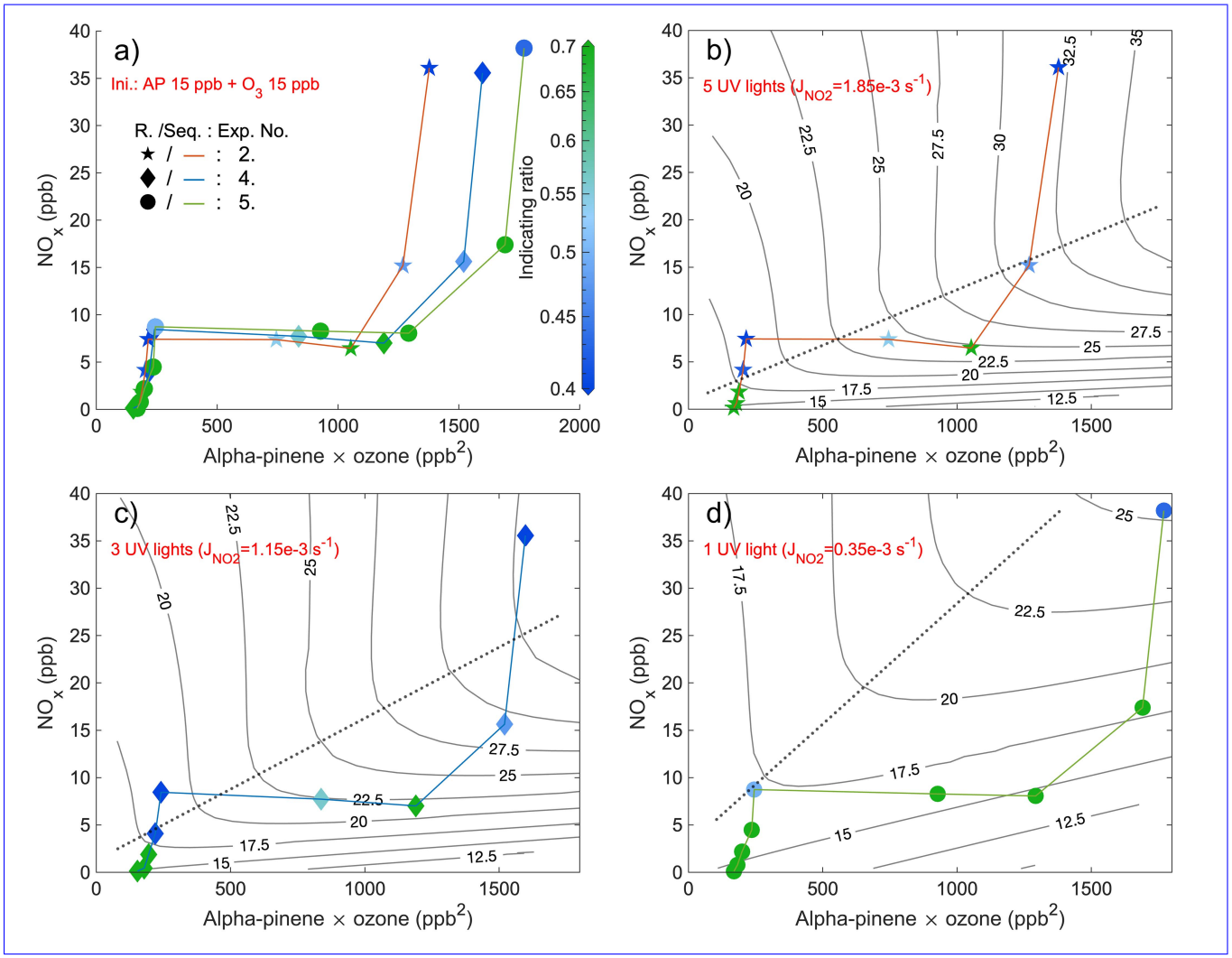

Figure A14. Steady state IR2 ($\frac{\sum \mathrm{HOM_{Mono,O>8}}}{\sum \mathrm{HOM_{ON,O>8}}}$) of experiments from three days with 5, 3, and 1 UV lights, respectively. X-axis is the multiplication of ~~measured (~~steady state ~~)~~ α-pinene and O_3 concentrations, while y-axis is the ~~measured (~~steady state ~~)~~ NO_x. The scatter points (exp. no. 2 (experiment number 2): star; exp. no. 4: diamond; exp. no. 5: round) are colored by values of IR2 (abbreviated as R. in the figure), and are connected by curves (exp. no. 2: orange; exp. no. 4: blue; exp. no. 5: green) showing the sequence (Seq.) of experimental stages. Panel a combines stages of all three days with the same initial (Ini.) inputs, and the rest three subplots respectively show the stages of experiments with different amount of UV lights. EKMA curves by the box model are in black lines and the dotted lines are corresponding ridge lines.

Table A1. Zero-VOC experiment conditions. Experiment numbers (No.) and number of total stages are shown in the first two columns. Input information include the number and NO_2 photolysis rates (J_{NO_2}) of UV lights ($\lambda \approx 400$ nm) and concentrations of O_3, α-pinene, and NO_x.

		Input			
Experiment *No.*	Number of stages	Number of lights	J_{NO_2} (s^{-1})	O_3 (ppb)	NO_x range (ppb)
Z1./Z2./Z3.	9/7/7	5	1.85×10^{-3}	10/15.5/22.5	0.7 – 44.5
Z4.	8	3	1.15×10^{-3}	15	0.7 – 44.5
Z5.	7	1	0.35×10^{-3}	15.5	0.7 – 44.5

~~The figures are shown~~From steady-state (ss in subscript) balance of the O_3 concentration, we can write the following expression:

$$\frac{d[O_3]}{dt} = J_{NO_2}[NO_2]_{ss} + \frac{[O_3]_{input} - [O_3]_{ss}}{\tau} - k_{O_3,NO}[O_3]_{ss}[NO]_{ss} = 0$$

where $\tau = \frac{2000\ L}{55\ L\ min^{-1}}$ is the residence time. O_3 has NO_2 photolysis ($J_{NO_2}[NO_2]_{ss}$) and its input ($\frac{[O_3]_{input}}{\tau}$) as sources, with reaction to NO ($-k_{O_3,NO}[O_3]_{ss}[NO]_{ss}$) and flush-out ($\frac{-[O_3]_{ss}}{\tau}$) as sinks. We can solve the equation to get NO_2 photolysis rate:

$$J_{NO_2} = \frac{k_{O_3,NO}[O_3]_{ss}[NO]_{ss} + \frac{[O_3]_{ss} - [O_3]_{input}}{\tau}}{[NO_2]_{ss}}$$

This expression can be used for each steady state to estimate J_{NO_2} in the corresponding experiment. ~~.~~

Table A2. ~~Chemical reactions~~ Reactions and their reaction rate coefficients used for the box model. Note that RO_2 represent all kinds of peroxy radicals, thus there are huge uncertainties regarding reaction rates. This model is only meant for simulating concentrations of O_3 and its precursors.

~~Chemical reactions~~ Reactions	Reaction rate coefficients [a]
1. $NO_2 + hv \xrightarrow{O_2} NO + O_3$	0.35/1.15/1.85 $\times 10^{-3}$
2. $O_3 + NO \rightarrow NO_2 + O_2$	1.8 $\times 10^{-14}$
3. $\alpha-pinene + O_3 \xrightarrow{O_2} RO_2 + OH$	8.7 $\times 10^{-17}$
4. $\alpha-pinene + OH \xrightarrow{O_2} RO_2$	5.5 $\times 10^{-11}$
5. $RO_2 + NO \rightarrow RO + NO_2$	1 $\times 10^{-11}$
6. $RO_2 + RO_2 \rightarrow 2RO + O_2$	8 $\times 10^{-13}$
7. $RO + O_2 \rightarrow HO_2$	Instantaneous
8. $NO + OH \rightarrow HNO_2$	4 $\times 10^{-11}$
9. $NO + OH \xrightarrow{O_2} HO_2 + NO_2$	1.2 $\times 10^{-13}$
10. $NO_2 + OH \rightarrow HNO_3$	4 $\times 10^{-11}$
11. $HO_2 + NO \rightarrow OH + NO_2$	1 $\times 10^{-11}$
12. $HO_2 + NO_2 \rightarrow HO_2NO_2$	3 $\times 10^{-14}$
13. $HO_2 + HO_2/RO_2 \rightarrow peroxides$	2 $\times 10^{-11}$
14. $RO_2 \rightarrow wall$ [b]	2.5 $\times 10^{-3}$

[a] Except the NO_2 photolysis and wall loss rates (s^{-1}), all the other reaction rates ($cm^3 \cdot s^{-1}$) are adapted from NIST (National Institute of Standards and Technology) Chemical Kinetics Database (more information see https://kinetics.nist.gov/kinetics/index.jsp)

[b] In our model, we only considered RO_2 with a wall loss lifetime of 400 s (Peräkylä et al., 2020).

Author contributions. ME, JZ, and JYZ designed the study. JZ, JYZ, YL, and VM conducted the experiments. JYZ analyzed the data and developed the model. ME, JZ, and DR supported the data analysis.

Competing interests. Douglas Worsnop works for Aerodyne Research, Inc.

Acknowledgements. The authors thank Lauriane Quéléver for the calibration of the NO_3-CIMS.

Financial support. This work was supported by funding from Academy of Finland (grant no. 345982) and the Jane and Aatos Erkko Foundation.

Open-access funding was provided by the Helsinki University Library.

References

Archer, S. L., Shultz, P. J., Warren, J. B., Hampl, V., and DeMaster, E. G.: Preparation of standards and measurement of nitric oxide, nitroxyl, and related oxidation products, Methods, 7, 21–34, https://doi.org/10.1006/meth.1995.1004, 1995.

Atkinson, R. and Arey, J.: Atmospheric degradation of volatile organic compounds, Chemical Reviews, 103, 4605–4638, https://doi.org/10.1021/cr0206420, 2003.

Atkinson, R., Baulch, D. L., Cox, R. A., Crowley, J. N., Hampson, R. F., Hynes, R. G., Jenkin, M. E., Rossi, M. J., and Troe, J.: Evaluated kinetic and photochemical data for atmospheric chemistry: Volume I - gas phase reactions of O_x, HO_x, NO_x and SO_x species, Atmospheric Chemistry and Physics, 4, 1461–1738, https://doi.org/10.5194/acp-4-1461-2004, 2004.

Bianchi, F., Kurtén, T., Riva, M., Mohr, C., Rissanen, M. P., Roldin, P., Berndt, T., Crounse, J. D., Wennberg, P. O., Mentel, T. F., Wildt, J., Junninen, H., Jokinen, T., Kulmala, M., Worsnop, D. R., Thornton, J. A., Donahue, N., Kjaergaard, H. G., and Ehn, M.: Highly oxygenated organic molecules (HOM) from gas-phase autoxidation involving peroxy radicals: A key contributor to atmospheric aerosol, Chemical Reviews, 119, 3472–3509, https://doi.org/10.1021/acs.chemrev.8b00395, 2019.

Boucher, O., Randall, D., Artaxo, P., Bretherton, C., Feingold, G., Forster, P., Kerminen, V.-M., Kondo, Y., Liao, H., and Lohmann, U.: Clouds and aerosols, in: Climate change 2013: The physical science basis. Contribution of working group I to the fifth assessment report of the intergovernmental panel on climate change, pp. 571–657, Cambridge University Press, 2013.

Chameides, W. L., Fehsenfeld, F., Rodgers, M. O., Cardelino, C., Martinez, J., Parrish, D., Lonneman, W., Lawson, D. R., Rasmussen, R. A., Zimmerman, P., Greenberg, J., Mlddleton, P., and Wang, T.: Ozone precursor relationships in the ambient atmosphere, Journal of Geophysical Research: Atmospheres, 97, 6037–6055, https://doi.org/10.1029/91JD03014, 1992.

Chapman, S.: A theory of upper-atmospheric ozone, Memoirs of the Royal Meteorological Society, 3, 103–125, https://cir.nii.ac.jp/crid/1572261549196038528, 1930.

Chipperfield, M. P., Bekki, S., Dhomse, S., Harris, N. R. P., Hassler, B., Hossaini, R., Steinbrecht, W., Thiéblemont, R., and Weber, M.: Detecting recovery of the stratospheric ozone layer, Nature, 549, 211–218, https://doi.org/10.1038/nature23681, 2017.

Crounse, J. D., Nielsen, L. B., Jørgensen, S., Kjaergaard, H. G., and Wennberg, P. O.: Autoxidation of organic compounds in the atmosphere, The Journal of Physical Chemistry Letters, 4, 3513–3520, https://doi.org/10.1021/jz4019207, 2013.

Crutzen, P. J.: The influence of nitrogen oxides on the atmospheric ozone content, Quarterly Journal of the Royal Meteorological Society, 96, 320–325, https://doi.org/10.1002/qj.49709640815, 1970.

Crutzen, P. J.: Ozone production rates in an oxygen-hydrogen-nitrogen oxide atmosphere, Journal of Geophysical Research, 76, 7311–7327, https://doi.org/10.1029/JC076i030p07311, 1971.

Dickerson, R. R., Kondragunta, S., Stenchikov, G., Civerolo, K. L., Doddridge, B. G., and Holben, B. N.: The impact of aerosols on solar ultraviolet radiation and photochemical smog, Science, 278, 827–830, https://doi.org/10.1126/science.278.5339.827, 1997.

Dodge, M. C.: Combined use of modeling techniques and smog chamber data to derive ozone-precursor relationships, in: International conference on photochemical oxidant pollution and its control: Proceedings, vol. 2, pp. 881–889, US Environmental Protection Agency, 1977.

Ehhalt, D., Prather, M., Dentener, F., Derwent, R., Dlugokencky, E., Holland, E., Isaksen, I., Katima, J., Kirchhoff, V., Matson, P., Midgley, P., Wang, M., Berntsen, T., Bey, I., Brasseur, G., Buja, L., Collins, W. J. J., Daniel, J., Demore, W. B. B., Derek, N., Dickerson, R., Etheridge, D., Feichter, J., Fraser, P., Friedl, R., Fuglestvedt, J., Gauss, M., Grenfell, L., Grübler, A., Harris, N., Hauglustaine, D., Horowitz, L., Jackman, C., Jacob, D., Jaeglé, L., Jain, A., Kanakidou, M., Karlsdottir, S., Ko, M., Kurylo, M., Lawrence, M., Logan, J. a. A., Manning,

M., Mauzerall, D., Mcconnell, J., Mickley, L., Montzka, S., Müller, J. F. F., Olivier, J., Pickering, K., Pitari, G., Roelofs, G. J. J., Rogers, H., Rognerud, B., Smith, S., Solomon, S., Staehelin, J., Steele, P., Stevenson, D., Sundet, J., Thompson, A., Weele, M. v., Kuhlmann, R. v., Wang, Y., Weisenstein, D., Wigley, T., Wild, O., Wuebbles, D., Yantosca, R., Joos, F., and Mcfarland, M.: Atmospheric chemistry and greenhouse gases, https://hal.science/hal-03333922, 2001.

Ehn, M., Thornton, J. A., Kleist, E., Sipilä, M., Junninen, H., Pullinen, I., Springer, M., Rubach, F., Tillmann, R., Lee, B., Lopez-Hilfiker, F., Andres, S., Acir, I.-H., Rissanen, M., Jokinen, T., Schobesberger, S., Kangasluoma, J., Kontkanen, J., Nieminen, T., Kurtén, T., Nielsen, L. B., Jørgensen, S., Kjaergaard, H. G., Canagaratna, M., Maso, M. D., Berndt, T., Petäjä, T., Wahner, A., Kerminen, V.-M., Kulmala, M., Worsnop, D. R., Wildt, J., and Mentel, T. F.: A large source of low-volatility secondary organic aerosol, Nature, 506, 476–479, https://doi.org/10.1038/nature13032, 2014.

Graus, M., Müller, M., and Hansel, A.: High resolution PTR-TOF: Quantification and formula confirmation of VOC in real time, Journal of the American Society for Mass Spectrometry, 21, 1037–1044, https://doi.org/10.1016/j.jasms.2010.02.006, 2010.

Gruijl, F. d. and Leun, J.: Environment and health: 3. Ozone depletion and ultraviolet radiation, CMAJ, 163, 851–855, https://www.cmaj.ca/content/163/7/851, 2000.

Haagen-Smit, A. J., Bradley, C. E., and Fox, M. M.: Ozone formation in photochemical oxidation of organic substances, Industrial & Engineering Chemistry, 45, 2086–2089, https://doi.org/10.1021/ie50525a044, 1953.

Hammer, M.-U., Vogel, B., and Vogel, H.: Findings on H_2O_2/HNO_3 as an indicator of ozone sensitivity in Baden-Württemberg, Berlin-Brandenburg, and the Po valley based on numerical simulations, Journal of Geophysical Research Atmospheres, 107, https://doi.org/10.1029/2000JD000211, 2002.

Hansel, A., Jordan, A., Holzinger, R., Prazeller, P., Vogel, W., and Lindinger, W.: Proton transfer reaction mass spectrometry: on-line trace gas analysis at the ppb level, International Journal of Mass Spectrometry and Ion Processes, 149-150, 609–619, https://doi.org/10.1016/0168-1176(95)04294-U, 1995.

Harris, G. W., Carter, W. P. L., Winer, A. M., Pitts, J. N., Platt, U., and Perner, D.: Observations of nitrous acid in the Los Angeles atmosphere and implications for predictions of ozone-precursor relationships, Environmental Science & Technology, 16, 414–419, https://doi.org/10.1021/es00101a009, 1982.

He, X.-C., Shen, J., Iyer, S., Juuti, P., Zhang, J., Koirala, M., Kytökari, M. M., Worsnop, D. R., Rissanen, M., Kulmala, M., Maier, N. M., Mikkilä, J., Sipilä, M., and Kangasluoma, J.: Characterisation of the multi-scheme chemical ionisation inlet-2 and the detection of gaseous iodine species, Atmospheric Measurement Techniques Discussions, pp. 1–48, https://doi.org/10.5194/amt-2023-30, 2023.

Jokinen, T., Sipilä, M., Junninen, H., Ehn, M., Lönn, G., Hakala, J., Petäjä, T., Mauldin, R. L. I., Kulmala, M., and Worsnop, D. R.: Atmospheric sulphuric acid and neutral cluster measurements using CI-APi-TOF, Atmospheric Chemistry and Physics, 12, 4117–4125, https://doi.org/10.5194/acp-12-4117-2012, 2012.

Jordan, A., Haidacher, S., Hanel, G., Hartungen, E., Märk, L., Seehauser, H., Schottkowsky, R., Sulzer, P., and Märk, T. D.: A high resolution and high sensitivity proton-transfer-reaction time-of-flight mass spectrometer (PTR-TOF-MS), International Journal of Mass Spectrometry, 286, 122–128, https://doi.org/10.1016/j.ijms.2009.07.005, 2009.

Junninen, H., Ehn, M., Petäjä, T., Luosujärvi, L., Kotiaho, T., Kostiainen, R., Rohner, U., Gonin, M., Fuhrer, K., Kulmala, M., and Worsnop, D. R.: A high-resolution mass spectrometer to measure atmospheric ion composition, Atmospheric Measurement Techniques, 3, 1039–1053, https://doi.org/10.5194/amt-3-1039-2010, 2010.

Kelly, F. J. and Fussell, J. C.: Air pollution and public health: emerging hazards and improved understanding of risk, Environmental Geochemistry and Health, 37, 631–649, https://doi.org/10.1007/s10653-015-9720-1, 2015.

Kinosian, J. R.: Ozone-precursor relationships from EKMA diagrams, Environmental Science & Technology, 16, 880–883, https://doi.org/10.1021/es00106a011, 1982.

Kleinman, L. I., Daum, P. H., Lee, Y.-N., Nunnermacker, L. J., Springston, S. R., Weinstein-Lloyd, J., and Rudolph, J.: Ozone production efficiency in an urban area, Journal of Geophysical Research: Atmospheres, 107, ACH 23–1, https://doi.org/10.1029/2002JD002529, 2002.

Krechmer, J. E., Day, D. A., and Jimenez, J. L.: Always lost but never forgotten: Gas-phase wall losses are important in all teflon nnvironmental chambers, Environmental Science & Technology, 54, 12 890–12 897, https://doi.org/10.1021/acs.est.0c03381, 2020.

Kürten, A., Rondo, L., Ehrhart, S., and Curtius, J.: Calibration of a chemical ionization mass spectrometer for the measurement of gaseous sulfuric acid, The Journal of Physical Chemistry A, 116, 6375–6386, https://doi.org/10.1021/jp212123n, 2012.

Kürten, A., Jokinen, T., Simon, M., Sipilä, M., Sarnela, N., Junninen, H., Adamov, A., Almeida, J., Amorim, A., Bianchi, F., Breitenlechner, M., Dommen, J., Donahue, N. M., Duplissy, J., Ehrhart, S., Flagan, R. C., Franchin, A., Hakala, J., Hansel, A., Heinritzi, M., Hutterli, M., Kangasluoma, J., Kirkby, J., Laaksonen, A., Lehtipalo, K., Leiminger, M., Makhmutov, V., Mathot, S., Onnela, A., Petäjä, T., Praplan, A. P., Riccobono, F., Rissanen, M. P., Rondo, L., Schobesberger, S., Seinfeld, J. H., Steiner, G., Tomé, A., Tröstl, J., Winkler, P. M., Williamson, C., Wimmer, D., Ye, P., Baltensperger, U., Carslaw, K. S., Kulmala, M., Worsnop, D. R., and Curtius, J.: Neutral molecular cluster formation of sulfuric acid–dimethylamine observed in real time under atmospheric conditions, Proceedings of the National Academy of Sciences, 111, 15 019–15 024, https://doi.org/10.1073/pnas.1404853111, 2014.

Lelieveld, J. and Dentener, F.: What controls tropospheric ozone?, Journal of Geophysical Research: Atmospheres, 105, https://doi.org/10.1029/1999JD901011, 2000.

Liu, C. and Shi, K.: A review on methodology in O_3-NO_x-VOC sensitivity study, Environmental Pollution, 291, 118 249, https://doi.org/10.1016/j.envpol.2021.118249, 2021.

Madronich, S., Hastie, D. R., Ridley, B. A., and Schiff, H. I.: Measurement of the photodissociation coefficient of NO_2 in the atmosphere. I - Method and surface measurements, Journal of Atmospheric Chemistry, 1, 3–25, https://doi.org/10.1007/BF00113977, 1983.

Martin, R., Fiore, A., and Donkelaar, A.: Space-based diagnosis of surface ozone sensitivity to anthropogenic emissions, Geophys. Res. Lett, 31, https://doi.org/10.1029/2004GL019416, 2004.

Melkonyan, A. and Kuttler, W.: Long-term analysis of NO, NO_2 and O_3 concentrations in North Rhine-Westphalia, Germany, Atmospheric Environment, 60, 316–326, https://doi.org/10.1016/j.atmosenv.2012.06.048, 2012.

Meyer Jr, E. L., Summerhays, J. P., and Freas, W.: Uses, limitations, and technical basis of procedures for quantifying relationships between photochemical oxidants and precursors, in: EPA-450/2-77-021a, Environmental Protection Agency Research Triangle Park, NC, 1977.

Nuvolone, D., Petri, D., and Voller, F.: The effects of ozone on human health, Environmental Science and Pollution Research, 25, 8074–8088, https://doi.org/10.1007/s11356-017-9239-3, 2018.

Pathak, R. K., Stanier, C. O., Donahue, N. M., and Pandis, S. N.: Ozonolysis of α-pinene at atmospherically relevant concentrations: Temperature dependence of aerosol mass fractions (yields), Journal of Geophysical Research: Atmospheres, 112, 2007.

Peräkylä, O., Riva, M., Heikkinen, L., Quéléver, L., Roldin, P., and Ehn, M.: Experimental investigation into the volatilities of highly oxygenated organic molecules (HOMs), Atmospheric Chemistry and Physics, 20, 649–669, https://doi.org/10.5194/acp-20-649-2020, 2020.

Riva, M., Heikkinen, L., Bell, D. M., Peräkylä, O., Zha, Q., Schallhart, S., Rissanen, M. P., Imre, D., Petäjä, T., Thornton, J. A., Zelenyuk, A., and Ehn, M.: Chemical transformations in monoterpene-derived organic aerosol enhanced by inorganic composition, npj Climate and Atmospheric Science, 2, 1–9, https://doi.org/10.1038/s41612-018-0058-0, 2019a.

Riva, M., Rantala, P., Krechmer, J. E., Peräkylä, O., Zhang, Y., Heikkinen, L., Garmash, O., Yan, C., Kulmala, M., Worsnop, D., and Ehn, M.: Evaluating the performance of five different chemical ionization techniques for detecting gaseous oxygenated organic species, Atmospheric Measurement Techniques, 12, 2403–2421, https://doi.org/10.5194/amt-12-2403-2019, 2019b.

Sandermann, H.: Ozone and plant health, Annual Review of Phytopathology, 34, 347–366, https://doi.org/10.1146/annurev.phyto.34.1.347, 1996.

Seinfeld, J. H. and Pandis, S. N.: Atmospheric chemistry and physics: From air pollution to climate change, John Wiley & Sons, 2016.

Seviour, W. J. M.: Good ozone, bad ozone and the Southern Ocean, Nature Climate Change, 12, 316–317, https://doi.org/10.1038/s41558-022-01322-8, 2022.

Sicard, P., De Marco, A., Agathokleous, E., Feng, Z., Xu, X., Paoletti, E., Rodriguez, J. J. D., and Calatayud, V.: Amplified ozone pollution in cities during the COVID-19 lockdown, Science of The Total Environment, 735, 139 542, https://doi.org/10.1016/j.scitotenv.2020.139542, 2020.

Sillman, S.: The relation between ozone, NO_x and hydrocarbons in urban and polluted rural environments, Atmospheric Environment, 33, 1821–1845, https://doi.org/10.1016/S1352-2310(98)00345-8, 1999.

Sillman, S., Logan, J. A., and Wofsy, S. C.: The sensitivity of ozone to nitrogen oxides and hydrocarbons in regional ozone episodes, Journal of Geophysical Research: Atmospheres, 95, 1837–1851, https://doi.org/10.1029/JD095iD02p01837, 1990.

Staehelin, J., Harris, N. R. P., Appenzeller, C., and Eberhard, J.: Ozone trends: A review, Reviews of Geophysics, 39, 231–290, https://doi.org/10.1029/1999RG000059, 2001.

Stolarski, R. S. and Cicerone, R. J.: Stratospheric chlorine: a possible sink for ozone, Canadian Journal of Chemistry, 52, 1610–1615, https://doi.org/10.1139/v74-233, 1974.

Tang, X., Li, J., and Chen, D.: Summertime photochemical pollution in Beijing, LOCAL AIR POLLUTION IN FAST DEVELOPING COUNTRIES, 1410, 1465, 1995.

Tiao, G. C., Box, G. E. P., and Hamming, W. J.: Analysis of Los Angeles photochemical smog data: a statistical overview, Journal of the Air Pollution Control Association, 25, 260–268, https://doi.org/10.1080/00022470.1975.10470082, 1975.

Trainer, M., Parrish, D. D., Buhr, M. P., Norton, R. B., Fehsenfeld, F. C., Anlauf, K. G., Bottenheim, J. W., Tang, Y. Z., Wiebe, H. A., Roberts, J. M., Tanner, R. L., Newman, L., Bowersox, V. C., Meagher, J. F., Olszyna, K. J., Rodgers, M. O., Wang, T., Berresheim, H., Demerjian, K. L., and Roychowdhury, U. K.: Correlation of ozone with NO_y in photochemically aged air, Journal of Geophysical Research: Atmospheres, 98, 2917–2925, https://doi.org/10.1029/92JD01910, 1993.

Wang, T., Ding, A., Gao, J., and Wu, W. S.: Strong ozone production in urban plumes from Beijing, China, Geophysical Research Letters, 33, https://doi.org/10.1029/2006GL027689, 2006.

Wang, T., Xue, L., Brimblecombe, P., Lam, Y. F., Li, L., and Zhang, L.: Ozone pollution in China: A review of concentrations, meteorological influences, chemical precursors, and effects, Science of The Total Environment, 575, 1582–1596, https://doi.org/10.1016/j.scitotenv.2016.10.081, 2017.

Yan, C., Nie, W., Äijälä, M., Rissanen, M. P., Canagaratna, M. R., Massoli, P., Junninen, H., Jokinen, T., Sarnela, N., Häme, S. A. K., Schobesberger, S., Canonaco, F., Yao, L., Prévôt, A. S. H., Petäjä, T., Kulmala, M., Sipilä, M., Worsnop, D. R., and Ehn, M.: Source characterization of highly oxidized multifunctional compounds in a boreal forest environment using positive matrix factorization, Atmospheric Chemistry and Physics, 16, 12 715–12 731, https://doi.org/10.5194/acp-16-12715-2016, 2016.

Yan, C., Nie, W., Vogel, A. L., Dada, L., Lehtipalo, K., Stolzenburg, D., Wagner, R., Rissanen, M. P., Xiao, M., Ahonen, L., Fischer, L., Rose, C., Bianchi, F., Gordon, H., Simon, M., Heinritzi, M., Garmash, O., Roldin, P., Dias, A., Ye, P., Hofbauer, V., Amorim, A.,

Bauer, P. S., Bergen, A., Bernhammer, A.-K., Breitenlechner, M., Brilke, S., Buchholz, A., Mazon, S. B., Canagaratna, M. R., Chen, X., Ding, A., Dommen, J., Draper, D. C., Duplissy, J., Frege, C., Heyn, C., Guida, R., Hakala, J., Heikkinen, L., Hoyle, C. R., Jokinen, T., Kangasluoma, J., Kirkby, J., Kontkanen, J., Kürten, A., Lawler, M. J., Mai, H., Mathot, S., Mauldin, R. L., Molteni, U., Nichman, L., Nieminen, T., Nowak, J., Ojdanic, A., Onnela, A., Pajunoja, A., Petäjä, T., Piel, F., Quéléver, L. L. J., Sarnela, N., Schallhart, S., Sengupta, K., Sipilä, M., Tomé, A., Tröstl, J., Väisänen, O., Wagner, A. C., Ylisirniö, A., Zha, Q., Baltensperger, U., Carslaw, K. S., Curtius, J., Flagan, R. C., Hansel, A., Riipinen, I., Smith, J. N., Virtanen, A., Winkler, P. M., Donahue, N. M., Kerminen, V.-M., Kulmala, M., Ehn, M., and Worsnop, D. R.: Size-dependent influence of NO_x on the growth rates of organic aerosol particles, Science Advances, 6, eaay4945, https://doi.org/10.1126/sciadv.aay4945, 2020.

Zhao, J., Häkkinen, E., Graeffe, F., Krechmer, J. E., Canagaratna, M. R., Worsnop, D. R., Kangasluoma, J., and Ehn, M.: A combined gas- and particle-phase analysis of highly oxygenated organic molecules (HOMs) from α-pinene ozonolysis, Atmospheric Chemistry and Physics, 23, 3707–3730, https://doi.org/10.5194/acp-23-3707-2023, 2023a.

Zhao, J., Mickwitz, V., Luo, Y., Häkkinen, E., Graeffe, F., Zhang, J., Timonen, H., Canagaratna, M., Krechmer, J. E., Zhang, Q., Kulmala, M., Kangasluoma, J., Worsnop, D., and Ehn, M.: Characterization of the vaporization inlet for aerosols (VIA) for online measurements of particulate highly oxygenated organic molecules (HOMs), EGUsphere, pp. 1–21, https://doi.org/10.5194/egusphere-2023-1146, 2023b.